bioRxiv preprint doi: https://doi.org/10.1101/2023.09.30.560314; this version posted October 2, 2023. The copyright holder for this preprint (which was not certified by peer review) is the author/funder, who has granted bioRxiv a license to display the preprint in perpetuity. It is made available under aCC-BY-NC-ND 4.0 International license.

Research Paper

ATF7IP2/MCAF2 directs H3K9 methylation and meiotic gene regulation in the male germline

Kris G. Alavattam[1, 2, 8], Jasmine M. Esparza[3, 8], Mengwen Hu[1, 3, 8], Ryuki Shimada[4, 8], Anna R. Kohrs[1], Hironori Abe[1, 3, 4], Yasuhisa Munakata[1, 3], Kai Otsuka[3], Saori Yoshimura[4], Yuka Kitamura[3], Yu-Han Yeh[1, 3], Yueh-Chiang Hu[1, 7], Jihye Kim[5], Paul R. Andreassen[6, 7], Kei-ichiro Ishiguro[4], and Satoshi H. Namekawa[1, 3, 7]

[1] Reproductive Sciences Center, Division of Developmental Biology, Cincinnati Children's Hospital Medical Center, Cincinnati, Ohio 45229, USA

[2] Basic Sciences Division, Fred Hutchinson Cancer Center, Seattle, Washington 98109, USA

[3] Department of Microbiology and Molecular Genetics, University of California, Davis, California 95616, USA

[4] Department of Chromosome Biology, Institute of Molecular Embryology and Genetics (IMEG), Kumamoto University, Kumamoto, 860-0811, Japan

[5] Laboratory of Chromosome Dynamics, Institute of Molecular and Cellular Biosciences, University of Tokyo, 1-1-1, Yayoi, Tokyo, 113-0032, Japan

[6] Division of Experimental Hematology and Cancer Biology, Cincinnati Children's Hospital Medical Center, Cincinnati, Ohio 45229, USA

[7] Department of Pediatrics, University of Cincinnati College of Medicine, Cincinnati, Ohio 49229, USA

[8] These authors contributed equally to this work.

Corresponding authors:

bioRxiv preprint doi: https://doi.org/10.1101/2023.09.30.560314; this version posted October 2, 2023. The copyright holder for this preprint (which was not certified by peer review) is the author/funder, who has granted bioRxiv a license to display the preprint in perpetuity. It is made available under aCC-BY-NC-ND 4.0 International license.

Kei-ichiro Ishiguro ishiguro@kumamoto-u.ac.jp

Satoshi H. Namekawa snamekawa@ucdavis.edu

Key words: Meiosis, Constitutive Heterochromatin, H3K9me3, Meiotic Sex Chromosome Inactivation, Gene activation, ATF7IP2/MCAF2

Abstract

H3K9 tri-methylation (H3K9me3) plays emerging roles in gene regulation, beyond its accumulation on pericentric constitutive heterochromatin. It remains a mystery why and how H3K9me3 undergoes dynamic regulation in male meiosis. Here, we identify a novel, critical regulator of H3K9 methylation and spermatogenic heterochromatin organization: the germline-specific protein ATF7IP2 (MCAF2). We show that, in male meiosis, ATF7IP2 amasses on autosomal and X pericentric heterochromatin, spreads through the entirety of the sex chromosomes, and accumulates on thousands of autosomal promoters and retrotransposon loci. On the sex chromosomes, which undergo meiotic sex chromosome inactivation (MSCI), the DNA damage response pathway recruits ATF7IP2 to X pericentric heterochromatin, where it facilitates the recruitment of SETDB1, a histone methyltransferase that catalyzes H3K9me3. In the absence of ATF7IP2, male germ cells are arrested in meiotic prophase I. Analyses of ATF7IP2-deficient meiosis reveal the protein's essential roles in the maintenance of MSCI, suppression of retrotransposons, and global upregulation of autosomal genes. We propose that ATF7IP2 is a downstream effector of the DDR pathway in meiosis that coordinates the organization of heterochromatin and gene regulation through the spatial regulation of SETDB1-mediated H3K9me3 deposition.

bioRxiv preprint doi: https://doi.org/10.1101/2023.09.30.560314; this version posted October 2, 2023. The copyright holder for this preprint (which was not certified by peer review) is the author/funder, who has granted bioRxiv a license to display the preprint in perpetuity. It is made available under aCC-BY-NC-ND 4.0 International license.

Introduction

Constitutive heterochromatin forms mainly at pericentromeres and is maintained to ensure genome stability. A hallmark of constitutive heterochromatin is histone H3K9 tri-methylation (H3K9me3) (Saksouk et al. 2015). It was initially considered a static histone mark due to its stable accumulation on tandem satellite repeats at pericentric heterochromatin (PCH); however, a growing literature reveals that H3K9me3—particularly H3K9me3 mediated by the histone methyltransferase SETDB1—has broad, dynamic roles in suppressing developmental regulator genes and endogenous retroviruses in embryonic stem cells (Bilodeau et al. 2009; Matsui et al. 2010), thereby defining cellular identities in somatic development (Becker et al. 2016; Nicetto and Zaret 2019).

An essential factor in the germline, SETDB1 is required for gene regulation, the suppression of transposable elements (TEs), and the control of meiotic chromosome behavior (Liu et al. 2014; Hirota et al. 2018; Mochizuki et al. 2018; Cheng et al. 2021). The redundant H3K9me3 methyltransferases SUV39H1 and SUV39H2 are also required for male meiosis (Peters et al. 2001). Thus, the regulation of H3K9me3 is critical in male meiosis, where constitutive heterochromatin is remodeled to undergo synapsis and meiotic recombination on homologous chromosomes (Scherthan et al. 2014; Berrios 2017; Maezawa et al. 2018a). However, it remains a mystery why and how H3K9me3 undergoes dynamic regulation in male meiosis.

In addition to its roles at PCH, H3K9me3 is subject to dynamic temporal and spatial regulation on the male sex chromosomes as they undergo meiotic sex chromosome inactivation

bioRxiv preprint doi: https://doi.org/10.1101/2023.09.30.560314; this version posted October 2, 2023. The copyright holder for this preprint (which was not certified by peer review) is the author/funder, who has granted bioRxiv a license to display the preprint in perpetuity. It is made available under aCC-BY-NC-ND 4.0 International license.

(MCSI) (Turner 2015; Alavattam et al. 2021). An essential event in the male germline, MSCI is initiated and maintained by a DNA damage response (DDR) pathway (Ichijima et al. 2011; Royo et al. 2013; Abe et al. 2022). Downstream of the DDR, SETDB1 establishes H3K9me3 on the sex chromosome and regulates MSCI (Hirota et al. 2018). SETDB1 is expressed in a broad range of cells, but there is a major knowledge gap as to how SETDB1 and H3K9me3 function in meiosis.

Here, we identify Activating transcription factor 7 interacting protein 2 (ATF7IP2), also known as MBD1-containing chromatin-associated factor 2 (MCAF2), as a novel, critical regulator of SETDB1's spatiotemporal activity, H3K9 methylation, and global spermatogenic gene regulation. We identified ATF7IP2 based on its gene expression in the germline. In the midst of our investigation, an IP-mass spectrometry analysis identified ATF7IP2 as a SETDB1-binding protein (Hirota et al. 2018), lending the factor further contextual significance. In mitotically cycling cells, its homolog ATF7IP (MCAF1) regulates SETDB1 for H3K9me3 establishment and transcriptional silencing (Ichimura et al. 2005; Timms et al. 2016; Tsusaka et al. 2019; Tsusaka et al. 2020). We show that ATF7IP2 is a counterpart to ATF7IP that is highly expressed in the germline and essential in male meiosis, revealing roles for ATF7IP2 in MSCI, global meiotic gene regulation, and the fine-tuning of retrotransposon-derived loci such as endogenous retroviruses. By uncovering ATF7IP2's germline functions, our study clarifies the regulatory logic for dynamic H3K9me3 deposition—and thus heterochromatin—in the male germline.

bioRxiv preprint doi: https://doi.org/10.1101/2023.09.30.560314; this version posted October 2, 2023. The copyright holder for this preprint (which was not certified by peer review) is the author/funder, who has granted bioRxiv a license to display the preprint in perpetuity. It is made available under aCC-BY-NC-ND 4.0 International license.

Results

ATF7IP2 is highly expressed in male meiosis and accumulates on heterochromatin

To understand the meiosis-specific regulation of H3K9me3, we focused on *Atf7ip2* (*Mcaf2*), a gene that is highly expressed in male meiosis as evidenced in RNA-seq datasets for germ cell development and spermatogenesis (Seisenberger et al. 2012; Hasegawa et al. 2015; Maezawa et al. 2018b) (Fig. 1A). *Atf7ip2* expression is low in male germ cells until the stage of meiosis, at which point it is highly upregulated in meiotic pachytene spermatocytes (Fig. 1A). On the other hand, its homolog *Atf7ip* (*Mcaf1*), which functions in mitotically dividing/somatic cells (Ichimura et al. 2005; Timms et al. 2016), is highly expressed in primordial germ cells and spermatogonia but is downregulated in pachytene spermatocytes. Among various tissues, *Atf7ip2* is highly expressed in testes (Supplemental Fig. S1A). Furthermore, mouse ATF7IP2 has high homology with human ATF7IP2 (Supplemental Fig. S1B), except for its long N-terminal amino acid tail, and ATF7IP2 is highly expressed in human testes' meiotic spermatocytes (Supplemental Fig. S1C). These results raise the possibility that ATF7IP2 is an evolutionarily conserved counterpart to ATF7IP that is highly expressed in late stages of spermatogenesis.

To understand the regulatory mechanism for *Atf7ip2* expression, we examined the genomic distribution of MEIOSIN and STRA8, both transcription factors that heterodimerize to initiate meiosis-specific transcription (Kojima et al. 2019; Ishiguro et al. 2020). We observed MEIOSIN and STRA8 peaks at the *Atf7ip2* transcription start site (TSS) in preleptotene-enriched testes (the preleptotene stage is a liminal stage for germ cells transitioning from mitosis to meiotic prophase I) [Fig. 1B, reanalysis of (Ishiguro et al. 2020)]. These peaks coincide with the accumulation of RNA polymerase II (POLII) and Cap Analysis of Gene Expression (CAGE)

bioRxiv preprint doi: https://doi.org/10.1101/2023.09.30.560314; this version posted October 2, 2023. The copyright holder for this preprint (which was not certified by peer review) is the author/funder, who has granted bioRxiv a license to display the preprint in perpetuity. It is made available under aCC-BY-NC-ND 4.0 International license.

signals in postnatal day 10.5 (P10.5) testes, which are enriched for preleptotene spermatocytes [Fig. 1B, reanalysis of (Li et al. 2013)]. In support of a role for MEIOSIN and STRA8 in *Atf7ip2* expression, *Atf7ip2* was downregulated in *Stra8*$^{-/-}$ and *Meiosin*$^{-/-}$ testes at P21 (Fig. 1C). In mouse testes, the first wave of meiosis occurs semi-synchronously, and *Atf7ip2* expression is at its highest in P18 testes, when late stages of meiotic prophase I spermatocytes first appear (Fig. 1C). Taken together, these results demonstrate that the expression of *Atf7ip2* is upregulated by MEIOSIN and STRA8, occurring amid a broad range of meiotic transcription (Kojima et al. 2019; Ishiguro et al. 2020).

To better understand the potential function of ATF7IP2, we investigated ATF7IP2 protein localization during stages of mouse male meiosis by performing immunofluorescence microscopy with chromosome spreads (Fig. 1D, E). In the leptotene stage of meiotic prophase I, when meiotic chromosome axes begin to condense, ATF7IP2 localizes on DAPI-discernible heterochromatin. ATF7IP2 continues to localize on all DAPI-discernible PCH through the zygotene stage, when homologs undergo synapsis; the pachytene stage, when homologs have completed synapsis; and the diplotene stage, when homologs begin desynapsis (Fig. 1E). Meiotic nuclei were staged through observations of chromosome axes as identified by SYCP3 (Alavattam et al. 2016; Alavattam et al. 2018), a component of meiotic axes, and the presence of the testis-specific histone variant H1T, which appears in mid pachytene nuclei and persists into haploid spermatids (Inselman et al. 2003). At the onset of the pachytene stage, the unsynapsed sex chromosomes undergo MSCI, and the most intense ATF7IP2 signals were observed on X-chromosome PCH (X-PCH) at that time (Fig. 1E, F). In the early and mid pachytene stages, ATF7IP2 localizes primarily on X-PCH; from the late pachytene stage onward, ATF7IP2

bioRxiv preprint doi: https://doi.org/10.1101/2023.09.30.560314; this version posted October 2, 2023. The copyright holder for this preprint (which was not certified by peer review) is the author/funder, who has granted bioRxiv a license to display the preprint in perpetuity. It is made available under aCC-BY-NC-ND 4.0 International license.

139 gradually spreads across the entirety of the sex chromosome domain (also referred to as the "XY
140 domain" or "XY chromatin,"). Thus, ATF7IP2 exhibits two distinct localization patterns in
141 meiotic prophase I: one is on the PCH of all chromosomes, and the other is intense accumulation
142 on X-PCH that proceeds to spread through the entirety of the XY chromatin.
143
144 *ATF7IP2 is required for male meiosis*
145 To test the function of ATF7IP2, we performed CRISPR-mediated genome editing to
146 generate *Atf7ip2* knockout mice. We targeted a guide RNA to a site within exon 4 (Fig. 2A),
147 which encodes a portion of the SETDB1-binding domain (SETDB1-BD) that is conserved
148 between ATF7IP2 and ATF7IP (Fig. 2B). We obtained three alleles with deletion lengths of,
149 respectively, 17, 31, and 169 bp. All caused *Atf7ip2* frameshift mutations, and all three
150 homozygous *Atf7ip2* mutants displayed consistent and obvious testicular defects. For subsequent
151 analyses, we selected the 17 bp-deletion allele as a representative; hereafter, the homozygous 17
152 bp-allele model is denoted *Atf7ip2*$^{-/-}$. *Atf7ip2*$^{-/-}$ male mice were viable but infertile, and had much
153 smaller testes compared to littermate controls (Fig. 2C, D, E). We confirmed the depletion of
154 ATF7IP2 proteins in *Atf7ip2*$^{-/-}$ spermatocytes via immunofluorescence microscopy
155 (Supplemental Fig. S2). Analyses of testicular tissue sections showed that *Atf7ip2*$^{-/-}$ testes were
156 devoid of haploid spermatids, and seminiferous tubules were smaller than in control testes (Fig.
157 2F). However, *Atf7ip2*$^{-/-}$ spermatocytes reached the stage when H1T is enriched, the mid
158 pachytene stage, indicating that *Atf7ip2*$^{-/-}$ spermatocytes are arrested and eliminated in meiotic
159 prophase I. Unlike *Atf7ip2*$^{-/-}$ males, *Atf7ip2*$^{-/-}$ female mice were fertile and, when crossed with
160 *Atf7ip2*$^{+/-}$ males, gave birth at Mendelian ratios (Supplemental Fig. S3). These results suggest

bioRxiv preprint doi: https://doi.org/10.1101/2023.09.30.560314; this version posted October 2, 2023. The copyright holder for this preprint (which was not certified by peer review) is the author/funder, who has granted bioRxiv a license to display the preprint in perpetuity. It is made available under aCC-BY-NC-ND 4.0 International license.

161 that the *Atf7ip2*$^{-/-}$ phenotype is caused by an essential, male-specific event in the germline that
162 has gone defective.
163
164 *Meiotic phenotypes in male Atf7ip2*$^{-/-}$ *mice*
165 To determine the function of ATF7IP2, we characterized the meiotic phenotype of
166 *Atf7ip2*$^{-/-}$ male mice in detail. We performed immunostaining to analyze chromosome spreads
167 from *Atf7ip2*$^{-/-}$ testes for a specific marker of the DDR: phosphorylated Serine 139 of the histone
168 variant H2AX (γH2AX). In the leptotene and zygotene stages, the DDR/checkpoint kinase
169 Ataxia Telangiectasia Mutated (ATM) triggers the formation of γH2AX domains throughout
170 nuclei in response to programmed double-stranded breaks (DSBs; induced by the topoisomerase-
171 related enzyme SPO11); with the completion of DNA repair and concomitant autosomal
172 synapsis, γH2AX disappears from autosomes (Mahadevaiah et al. 2001; Bellani et al. 2005). In
173 the latter steps of this process, Ataxia Telangiectasia and Rad3-Related (ATR), another
174 DDR/checkpoint kinase, mediates γH2AX formation on unsynapsed chromatin; in normal
175 pachytene nuclei, this results in the confinement of γH2AX to the unsynapsed XY chromosomes,
176 an essential event in the initiation of MSCI (Royo et al. 2013). Thus, γH2AX staining, together
177 with SYCP3 staining, provides key insights into general meiotic phenotypes (Abe et al. 2018;
178 Alavattam et al. 2018). In *Atf7ip2*$^{-/-}$ spermatocytes, pan-nuclear γH2AX formation occurs
179 normally in the early/mid zygotene stage (Fig. 3A), and relative populations of zygotene
180 spermatocytes are comparable between *Atf7ip2*$^{-/-}$ testes and littermate controls (Fig. 3B). In the
181 *Atf7ip2*$^{-/-}$ pachytene spermatocytes, γH2AX formation on the XY chromosomes takes place (Fig.
182 3A); however, we noted a significant increase in the relative population of early/mid pachytene
183 spermatocytes, while diplotene spermatocytes were rare and largely depleted from *Atf7ip2*$^{-/-}$

bioRxiv preprint doi: https://doi.org/10.1101/2023.09.30.560314; this version posted October 2, 2023. The copyright holder for this preprint (which was not certified by peer review) is the author/funder, who has granted bioRxiv a license to display the preprint in perpetuity. It is made available under aCC-BY-NC-ND 4.0 International license.

184 testes (Fig. 3B). These analyses suggest that ATF7IP2 has a critical function as spermatocytes
185 transition from the pachytene to diplotene stages.
186
187 Following our established criteria for SYCP3- and γH2AX-based meiotic staging (Abe et
188 al. 2018; Alavattam et al. 2018), we analyzed γH2AX staining patterns in more detail. In *Atf7ip2*$^{-}$
189 $^{/-}$ early/mid pachytene spermatocytes, the removal of γH2AX from autosomes was delayed in
190 comparison to controls (Fig. 3C). In normal meiosis, γH2AX accumulates through the whole of
191 leptotene and early zygotene nuclei (Pattern I, Fig. 3A and 3C); as spermatocytes progress into
192 the late zygotene stage, γH2AX accumulation transitions from a pan-nuclear diffuse signal to
193 concentrated accumulation on the chromatin associated with unsynapsed chromosome axes,
194 albeit with partial signals remaining along synapsed autosomes (Pattern II); by the mid and late
195 pachytene stages, γH2AX is confined to XY chromatin, having largely disappeared from
196 autosomes (Pattern III). In *Atf7ip2*$^{-/-}$ early/mid pachytene spermatocytes, γH2AX remains on
197 autosomes longer than in littermate controls (Fig. 3C), suggesting that, in the absence of
198 ATF7IP2, autosomal DDR signaling is affected.
199
200 Following on this, we investigated the outcome of meiotic recombination by scoring the
201 numbers of MLH1 foci—which illuminate crossover sites—on chromosome axes. Numbers of
202 MLH1 foci were comparable between *Atf7ip2*$^{+/-}$ and *Atf7ip2*$^{-/-}$ H1T-positive mid/late pachytene
203 spermatocytes (Fig. 3D). While a recent study of a separate *Atf7ip2*$^{-/-}$ mouse line reported
204 reduced numbers of XY pseudoautosomal regions (PARs) with MLH1 foci (Shao et al. 2023),
205 our observations showed no significant difference in the proportions of MLH1-associated PARs
206 in *Atf7ip2*$^{+/-}$ and *Atf7ip2*$^{-/-}$ models (Fig. 3D). Next, we analyzed chromosome synapsis by

bioRxiv preprint doi: https://doi.org/10.1101/2023.09.30.560314; this version posted October 2, 2023. The copyright holder for this preprint (which was not certified by peer review) is the author/funder, who has granted bioRxiv a license to display the preprint in perpetuity. It is made available under aCC-BY-NC-ND 4.0 International license.

207 immunostaining for SYCP3 (a marker of both unsynapsed and synapsed axes) and SYCP1 (a
208 marker of only synapsed axes); we observed occasional but significant autosomal asynapsis in
209 *Atf7ip2*$^{-/-}$ pachytene spermatocytes: ~87% of *Atf7ip2*$^{-/-}$ pachytene nuclei evidenced complete
210 synapsis, while nearly all *Atf7ip2*$^{+/+}$ spermatocytes showed complete synapsis (Fig. 3E). On
211 occasion, the shapes of sex chromosome axes exhibited abnormal configurations, including
212 apparent looped synapsis ("bubbles"), synapsis with large portions of itself ("irregular"), and
213 synapsis at ends ("circular;" Fig. 3F); ~25% of *Atf7ip2*$^{-/-}$ pachytene nuclei demonstrated
214 abnormal sex chromosome synapsis (Fig. 3F). These results suggest that, although ATF7IP2 may
215 not play an outsized role in meiotic recombination, both DDR signaling and chromosome
216 synapsis are impaired to some extent in *Atf7ip2*$^{-/-}$ spermatocytes.
217
218 *ATF7IP2 directs SETDB1 and H3K9 methylation in male meiosis*
219 Because ATF7IP binds SETDB1 to regulate H3K9me3 in somatic cells (Ichimura et al.
220 2005), we suspected that ATF7IP2 regulates H3K9me3 during meiosis. In meiotic prophase I,
221 H3K9me3 accumulates on autosomal PCH and the sex chromosomes, where it is subject to
222 dynamic regulation as XY undergoes MSCI (van der Heijden et al. 2007); H3K9me3 on the sex
223 chromosomes is established by the methyltransferase SETDB1 (Hirota et al. 2018; Abe et al.
224 2022). Consistent with this, we observed normal H3K9me3 accumulation on autosomal PCH and
225 XY chromatin in wild-type pachytene nuclei (Fig. 4A). Through careful examination, we noted
226 multiple H3K9me3 accumulation patterns on the sex chromosome in the early pachytene stage of
227 wild-type spermatocytes, coming to recognize four general patterns: Class I, covering the
228 entirety of XY; Class II, covering the entirety of Y and X-PCH; Class III, covering X-PCH only;
229 and Class IV, absent from XY, i.e., no signal (Fig. 4A, B; Supplemental Fig. S4A). We evaluated

bioRxiv preprint doi: https://doi.org/10.1101/2023.09.30.560314; this version posted October 2, 2023. The copyright holder for this preprint (which was not certified by peer review) is the author/funder, who has granted bioRxiv a license to display the preprint in perpetuity. It is made available under aCC-BY-NC-ND 4.0 International license.

230 the proportions of patterns, finding that H3K9me3 enrichment on the XY domain was impaired
231 in the early pachytene stage of *Atf7ip2*$^{-/-}$ spermatocytes: 33% of nuclei showed essentially no
232 signal anywhere on the XY chromosomes (Class IV), a pattern that was not observed in any
233 *Atf7ip2*$^{+/+}$ early pachytene nuclei (Fig. 4A, B). In normal mid and late pachytene stages,
234 H3K9me3 is retained on X-PCH as it disappears from the remainder of XY chromatin (Fig. 4A),
235 presumably due to histone replacement and the incorporation of histone variant H3.3 (van der
236 Heijden et al. 2007). Then, in the normal diplotene stage, H3K9me3 signals promulgate through
237 the XY chromatin in a likely reflection of H3K9me3's *de novo* deposition on H3.3 (Fig. 4A).
238 However, in *Atf7ip2*$^{-/-}$ mid and late pachytene spermatocytes, H3K9me3 on X-PCH decreased,
239 and reestablishment through the entirety of XY did not take place in the diplotene stage (Fig. 4A,
240 C). Alongside the diplotene reestablishment of H3K9me3, H3K9me2 also accumulates on XY
241 chromatin; however, in *Atf7ip2*$^{-/-}$ diplotene spermatocytes, we noted a clear loss of H3K9me2
242 (Fig. 4D, E). Concomitant with these changes, in *Atf7ip2*$^{-/-}$ spermatocytes, we observed the
243 strong accumulation of H3K9 acetylation (H3K9ac), which counteracts H3K9 methylation, on
244 X-PCH (Supplemental Fig. S4B). On the other hand, proportions of H3K9me1 accumulation
245 patterns were unchanged between control and *Atf7ip2*$^{-/-}$ spermatocytes (Supplemental Fig. S4C,
246 D), highlighting a specific role for ATF7IP2 in the regulation of H3K9me2/3 and H3K9ac.
247 Together, these results indicate that ATF7IP2 is required for the establishment of H3K9me2/3 on
248 diplotene XY chromatin, consistent with the concurrent, dynamic localization of ATF7IP2 from
249 X-PCH through XY chromatin.
250
251 Given this, we hypothesized that ATF7IP2 regulates the spatiotemporal recruitment of
252 SETDB1, which mediates H3K9me3, to the sex chromosomes. In wild-type early and mid

bioRxiv preprint doi: https://doi.org/10.1101/2023.09.30.560314; this version posted October 2, 2023. The copyright holder for this preprint (which was not certified by peer review) is the author/funder, who has granted bioRxiv a license to display the preprint in perpetuity. It is made available under aCC-BY-NC-ND 4.0 International license.

253 pachytene nuclei, SETDB1 localizes on the XY chromosomes and is notably enriched on the X-
254 PCH. In corresponding *Atf7ip2*$^{-/-}$ spermatocytes, SETDB1 was not enriched on X-PCH,
255 localizing instead to sex chromosome-adjacent nucleoli (Fig. 4F). Consistent with this, *Atf7ip2*$^{-/-}$
256 X-PCH was less DAPI-intense compared to controls (Supplemental Fig. S5), suggesting a defect
257 in heterochromatin formation. We also noticed that the pachytene accumulation of SETDB1 on
258 autosomal PCH was disrupted in corresponding *Atf7ip2*$^{-/-}$ spermatocytes: In contrast to the
259 constrained, intense SETDB1 signals of wild-type samples, we observed diffuse SETDB1
260 signals through the whole of mutant nuclei (Fig. 4F). We also observed that, in *Setdb1*
261 conditionally deleted mutants driven by the germline-specific *Ddx4*-Cre (*Setdb1*-cKO) (Abe et
262 al. 2022), the accumulation of ATF7IP2 on X-PCH was significantly reduced (Supplemental Fig.
263 S6A). Taken together, these results indicate a pan-nuclear role for ATF7IP2 in the
264 spatiotemporal regulation of SETDB1; furthermore, at X-PCH, ATFIP2 and SETDB1 likely
265 operate in tandem, possibly as a protein complex.
266
267 A hallmark of normal MSCI is the sex chromosome-wide accumulation of γH2AX, and
268 γH2AX domain formation is tightly associated with the initiation and maintenance of MSCI
269 (Fernandez-Capetillo et al. 2003; Abe et al. 2022). γH2AX domain formation is directed by
270 MDC1, a γH2AX-binding protein and central mediator of the DDR, through a feed-forward
271 mechanism (Ichijima et al. 2011). We hypothesized that the accumulation of ATF7IP2 on XY
272 chromatin occurs downstream of MDC1. To test this, we stained for ATF7IP2 in *Mdc1*$^{-/-}$
273 spermatocytes, finding that, in the absence of MDC1, ATF7IP2 failed to concentrate on X-PCH
274 (Fig. 4G). Similarly, the accumulation of SETDB1 on X-PCH depended on MDC1
275 (Supplemental Fig. S6B). These results suggest that the MDC1-dependent DDR pathway

bioRxiv preprint doi: https://doi.org/10.1101/2023.09.30.560314; this version posted October 2, 2023. The copyright holder for this preprint (which was not certified by peer review) is the author/funder, who has granted bioRxiv a license to display the preprint in perpetuity. It is made available under aCC-BY-NC-ND 4.0 International license.

276 regulates ATF7IP2 and SETDB1 localization on the sex chromosomes. We infer that, in
277 pachytene spermatocytes, the MDC1-dependent DDR pathway recruits ATF7IP2, and thus
278 SETDB1, to X-PCH; in the subsequent diplotene stage, both factors spread through the XY
279 chromatin and, as this occurs, SETDB1 deposits pan-XY H3K9me2/3 (Fig. 4H, I). Corroborating
280 this model, we found that MDC1 accumulation on XY chromatin occurred independently of
281 ATF7IP2 or SETDB1 (Supplemental Fig. S6C, D).
282
283 To parse mechanisms related to ATF7IP2, we tested the localization of related factors. A
284 previous study suggested a role for the SETDB1-interacting protein TRIM28 as a linker between
285 the DDR pathway and SETDB1 (Hirota et al. 2018). However, we found that TRIM28 does not
286 localize on the sex chromosomes in wild-type meiosis (Supplemental Fig. S7A), which raises the
287 possibility that ATF7IP2 works independently of TRIM28 to link the DDR pathway and
288 SETDB1. In line with this possibility, TRIM28 is dispensable for male meiotic progression (Tan
289 et al. 2020). Downstream of the DDR pathway, the chromatin remodeler CHD4 is recruited to X-
290 PCH (Broering et al. 2014); in *Atf7ip2*$^{-/-}$ spermatocytes, CHD4 accumulation on X-PCH was
291 unchanged from controls (Supplemental Fig. S7B). The germline-specific Polycomb protein
292 SCML2 also accumulates on XY chromatin downstream of the DDR pathway; in *Atf7ip2*$^{-/-}$
293 spermatocytes, SCML2 localization did not differ from controls (Supplemental Fig. S7C, D).
294 These results suggest that the disfunction of ATF7IP2 is not related to the localization of
295 TRIM28, CHD4, and SCML2.
296
297 We also examined the localization of ATF7IP in *Atf7ip2*$^{-/-}$ spermatogenesis. In wild-type
298 tissue sections, ATF7IP was predominantly found in the nuclei of primary spermatocytes

bioRxiv preprint doi: https://doi.org/10.1101/2023.09.30.560314; this version posted October 2, 2023. The copyright holder for this preprint (which was not certified by peer review) is the author/funder, who has granted bioRxiv a license to display the preprint in perpetuity. It is made available under aCC-BY-NC-ND 4.0 International license.

(Supplemental Fig. S7E); more specifically, it localized to the X-PCH in wild-type pachytene spermatocytes (Supplemental Fig. S7F, G). Contrastingly, in *Atf7ip2*$^{-/-}$ pachytene spermatocytes, ATF7IP was absent from the X-PCH and, instead, localized to the XY PAR. These results demonstrate ATF7IP2 is essential for directing ATF7IP and SETDB1 to X-PCH in pachytene spermatocytes.

ATF7IP2 is required for meiotic gene regulation

Having established its meiotic phenotype and essential role in H3K9 methylation, we sought to investigate the function of ATF7IP2 in meiotic gene regulation. To this end, we performed single-cell RNA sequencing (scRNA-seq) analyses of whole testicular cells from *Atf7ip2*$^{-/-}$ mice and their *Atf7ip2*$^{+/+}$ littermates at P15. The cellular composition of the testis changes as development progresses, leading us to confirm that, in P15 testes, the first wave of spermatogenesis exhibited a similar cellular composition between *Atf7ip2*$^{+/+}$ and *Atf7ip2*$^{-/-}$ mice. Indeed, we observed this was the case until the mid-to-late pachytene stages, when defects appeared based on immunostaining against major markers of spermatogenesis, including ZBTB16, STRA8, SYCP3, γH2AX, and H1T (Supplemental Fig. S8).

Using the scRNA-seq data, we endeavored to determine when ATF7IP2 functions in wild-type spermatogenesis. Since ATF7IP2 expression was restricted to germ cells, scRNA-seq data derived from germ cell populations (spermatogonia and spermatocytes) were analyzed apart from those of testicular somatic cells (Sertoli cells, Leydig cells, peritubular myoid cells, endothelial cells, and hemocytes) (Fig. 5A; Supplemental Fig. S9A, B). Using the UMAP of scRNA-seq data from *Atf7ip2*$^{+/+}$ and *Atf7ip2*$^{-/-}$ germ cell populations, we identified 13 cell-type

bioRxiv preprint doi: https://doi.org/10.1101/2023.09.30.560314; this version posted October 2, 2023. The copyright holder for this preprint (which was not certified by peer review) is the author/funder, who has granted bioRxiv a license to display the preprint in perpetuity. It is made available under aCC-BY-NC-ND 4.0 International license.

322 clusters; the cluster numbers are based on the numbers of cells comprising each cluster: Cluster 0
323 is the largest, and Cluster 12 is the smallest (Fig. 5B, C; Supplemental Fig. S9C, D). Assessing
324 the expression of key marker genes for spermatogenesis with respect to the UMAP, we inferred
325 the developmental trajectory of P15 spermatogenesis (Fig. 5D). As suggested by the high
326 expression of *Gfra1*, Cluster 8 represented a population of undifferentiated spermatogonia,
327 including spermatogonial stem cells. Cluster 1 represented a population of differentiating
328 spermatogonia as indicated by the initial upregulation of *Stra8.* Clusters 6 and 7 represented cells
329 at the initiation of meiosis, consistent with the upregulation of *Meiosin* and *Stra8.* Cluster 11
330 represented a population of spermatocytes in early meiotic prophase as denoted by the
331 upregulation of *Prdm9.* Based on the expression of marker genes with respect to the UMAP, we
332 inferred that spermatogenesis progressed along the trajectory from Clusters 8 to 12. Although
333 *Atf7ip2* was expressed in a broad range of spermatogenic stages, its expression level was higher
334 in Clusters 7, 6, 11, and 5, all of which correspond to meiotic prophase (Fig. 5E). Given that
335 *Atf7ip2* is bound by MEIOSIN and STRA8 (Fig. 1B), it is possible that the expression of *Atf7ip2*
336 was boosted, rather than initiated, at the entry to meiosis. In contrast, *Atf7ip* is constitutively
337 expressed in spermatogenesis (Fig. 5E).
338
339 Next, we sought to understand when cell death takes place in *Atf7ip2*$^{-/-}$ spermatocytes.
340 Starting from Cluster 8 through to Cluster 5, the gene expression profiles for *Atf7ip2*$^{+/+}$ and
341 *Atf7ip2*$^{-/-}$ germ cell populations overlapped one another to a high degree (Fig. 5A, B), indicating
342 that *Atf7ip2*$^{-/-}$ spermatogenesis progressed until the stage of spermatogenesis that corresponds to
343 Cluster 5. However, we noticed certain subpopulations—Clusters 10, 0, 2, and 3, representing B
344 spermatogonia through to preleptotene cells—were more numerous in *Atf7ip2*$^{-/-}$ germ cells (Fig.

bioRxiv preprint doi: https://doi.org/10.1101/2023.09.30.560314; this version posted October 2, 2023. The copyright holder for this preprint (which was not certified by peer review) is the author/funder, who has granted bioRxiv a license to display the preprint in perpetuity. It is made available under aCC-BY-NC-ND 4.0 International license.

345 5C); the increased cluster sizes suggest that, in the absence of ATF7IP2, the entry into meiosis is
346 hampered. Furthermore, the subpopulation represented by Cluster 12 was present in *Atf7ip2*$^{+/+}$
347 germ cells but missing amid *Atf7ip2*$^{-/-}$ germ cells (Fig. 5B, C). Furthermore, in *Atf7ip2*$^{+/+}$ germ
348 cells, expression levels of sex-linked genes were abruptly downregulated in the transition from
349 Clusters 5 to 12 (Fig. 5G). Intriguingly, in *Atf7ip2*$^{-/-}$ cells, Cluster 5 was associated with a strong,
350 abrupt upregulation of sex-linked gene expression (Fig. 5G), suggesting that MSCI failure began
351 in the Cluster-5 subpopulation of *Atf7ip2*$^{-/-}$ cells. Thus, the loss of the Cluster-12 subpopulation
352 in *Atf7ip2*$^{-/-}$ testes was preceded by an ectopic upregulation of X and Y chromosomal genes in
353 Cluster 5 (Fig. 5G), indicating Clusters 5 and 12 represent pachytene spermatocytes.
354
355 Remarkably, gene enrichment analysis revealed that genes related to late spermatogenesis
356 (e.g., *Clgn, Hspa2, Piwil1,* and *Ldhc*) were highly expressed in the Cluster-12 subpopulation of
357 spermatocytes (Supplemental Fig. S9C, Table S1). Since those genes are known to be expressed
358 in the late pachytene stage onward, we infer Cluster 12 corresponds to cytologically defined late
359 pachytene spermatocytes. This is consistent with the cytological observation that *Atf7ip2*$^{-/-}$
360 spermatocytes progressed through early meiotic prophase but were eliminated via apoptosis at
361 the transition from the late pachytene to diplotene stages (Fig. 3B). Thus, ATF7IP2 is required
362 for spermatocytes to progress beyond the late pachytene stage represented by Cluster 12.
363
364 *ATF7IP2 binds broadly to the sex chromosomes and autosomal gene promoters*
365 To determine where ATF7IP2 binds the genome of wild-type pachytene spermatocytes,
366 we performed CUT&Tag for ATF7IP2 in two biological replicates. The replicates were highly
367 correlated (Supplemental Fig. S10A), allowing us to merge them for downstream analyses.

bioRxiv preprint doi: https://doi.org/10.1101/2023.09.30.560314; this version posted October 2, 2023. The copyright holder for this preprint (which was not certified by peer review) is the author/funder, who has granted bioRxiv a license to display the preprint in perpetuity. It is made available under aCC-BY-NC-ND 4.0 International license.

368 Analyses of ATF7IP2 coverage revealed 61,797 genome-wide regions of enriched ATF7IP2-
369 binding, i.e., "ATF7IP2 peaks" (Fig. 6A). We observed ATF7IP2 peaks on TSSs (26.7 %), gene
370 bodies (27.7 %), and intergenic regions (45.4 %). TSS peaks were enriched on autosomes, while
371 intergenic peaks were enriched on the sex chromosomes (Fig. 6A), suggesting distinct functions
372 for ATF7IP2 on the autosomes and sex chromosomes. Continuing to analyze wild-type
373 pachytene spermatocytes, we performed two-step clustering with ATF7IP2 peaks, regions of
374 H3K9me3 coverage, and regions of coverage for the active promoter mark H3K4me3, generating
375 three clusters (Fig. 6B). Cluster I regions (6,632) are associated with H3K4me3 deposition (Fig.
376 6B) on autosomes and at TSSs (Fig. 6C, D). Cluster II regions (22,579) are associated with broad
377 H3K9me3 enrichment (Fig. 6B); 70% of these regions are on the sex chromosomes (Fig. 6C),
378 mostly at intergenic regions and gene bodies (Fig. 6D); this is in line with the role of ATF7IP2 in
379 the regulation of H3K9me3 on the sex chromosomes. Cluster III regions (32,628) largely
380 represent autosomal intergenic regions and gene bodies (Fig. 6C, D).
381
382 Based on the enrichment of ATF7IP2 at TSSs, we sought to identify ATF7IP2-target
383 genes in pachytene spermatocytes. Our analyses revealed 4,917 autosomal genes and 270 sex
384 chromosomal genes (Supplemental Table S2). ATF7IP2 binds the promoters of a broad range of
385 genes required for meiotic prophase and spermiogenesis, including *Hormad1* and *Sycp3*, both
386 autosomal genes, as well as Y-linked *Zfy1*. These promoter peaks are associated with the active
387 histone modifications H3K4me3 and H3K27ac (Supplemental Fig. S10B). Next, using our
388 scRNA-seq data set for *Atf7ip2*$^{+/+}$ and *Atf7ip2*$^{-/-}$ pachytene spermatocytes, we sought to
389 understand the regulation of ATF7IP2-target genes. We detected the expression of 4,626
390 ATF7IP2-target genes on autosomes and 211 on the sex chromosomes. The autosomal genes

bioRxiv preprint doi: https://doi.org/10.1101/2023.09.30.560314; this version posted October 2, 2023. The copyright holder for this preprint (which was not certified by peer review) is the author/funder, who has granted bioRxiv a license to display the preprint in perpetuity. It is made available under aCC-BY-NC-ND 4.0 International license.

391 were downregulated in *Atf7ip2*$^{-/-}$ pachytene spermatocytes (Fig. 6E: Clusters 6 to 5, representing
392 the early-to-mid-pachytene stages). Because wild-type autosomal promoter peaks are associated
393 with H3K4me3, these results indicate that ATF7IP2 binds to and positively regulates the
394 expression of these genes. On the other hand, in *Atf7ip2*$^{-/-}$ pachytene spermatocytes, the 211 sex
395 chromosomal genes are highly upregulated in Cluster 5 (mid pachytene spermatocytes),
396 indicating that ATF7IP2 binds to and negatively regulates the expression of these genes. These
397 results reveal two separate functions for ATF7IP2 in pachytene spermatocytes: one for
398 autosomal gene expression and, contrastingly, another for sex chromosomal gene repression.
399
400 *ATF7IP2 directs meiotic gene regulation*
401 To elucidate gene regulatory mechanisms associated with ATF7IP2, we isolated
402 pachytene spermatocytes from *Atf7ip2*$^{+/+}$ and *Atf7ip2*$^{-/-}$ testes, verified their purity (Supplemental
403 Fig. S10D), performed bulk RNA-seq with spike-in controls, and analyzed the resulting
404 transcription data. In isolating the cells, we were surprised to observe that *Atf7ip2*$^{-/-}$
405 spermatocytes were smaller than their *Atf7ip2*$^{+/+}$ counterparts (Supplemental Fig. S10D). This
406 gross decrease in size suggests that, in *Atf7ip2*$^{-/-}$ spermatocytes, the pachytene transcriptional
407 burst (Maezawa et al. 2020) is compromised—a possibility consistent with the global
408 downregulation of ATF7IP2-bound autosomal genes detected with scRNA-seq.
409
410 Comparing the spike-in-normalized mutant and control RNA-seq data, we identified
411 8,507 autosomal differentially expressed genes (DEGs): 185 upregulated and 8,322
412 downregulated (Fig. 7A). To understand how autosomal DEGs are expressed during normal
413 spermatogenesis, we reanalyzed separate RNA-seq data taken from cell types sampled across

bioRxiv preprint doi: https://doi.org/10.1101/2023.09.30.560314; this version posted October 2, 2023. The copyright holder for this preprint (which was not certified by peer review) is the author/funder, who has granted bioRxiv a license to display the preprint in perpetuity. It is made available under aCC-BY-NC-ND 4.0 International license.

414 wild-type spermatogenesis (Maezawa et al. 2018b). The 185 upregulated genes displayed high
415 expression levels in wild-type spermatogonia but were suppressed in wild-type pachytene
416 spermatocytes (Supplemental Fig. S11A). Thus, their upregulation in *Atf7ip2*$^{-/-}$ pachytene
417 spermatocytes suggests an ectopic expression of normally repressed premeiotic genes. The top
418 Gene Ontology (GO) (Ashburner et al. 2000) enrichment terms for these genes are related to
419 immune-system functions (Supplemental Fig. S11B), suggesting that ATF7IP2 suppresses the
420 expression of immune genes in pachytene spermatocytes. In contrast, many of the 8,322
421 downregulated genes were highly expressed in wild-type pachytene spermatocytes
422 (Supplemental Fig. Fig. S11A), and the associated GO enrichment terms were related to
423 spermatogenesis (Supplemental Fig. S11B). These findings indicate that many spermatogenesis-
424 related genes fail to activate in *Atf7ip2*$^{-/-}$ pachytene spermatocytes. Shifting focus to the sex
425 chromosomes, we detected 528 DEGs associated with the *Atf7ip2*$^{-/-}$ pachytene X chromosome:
426 522 were upregulated in mutants relative to controls, while 6 were downregulated (Fig. 7A). On
427 the Y chromosome, 12 DEGs were upregulated, and we detected no downregulated DEGs (Fig.
428 7A). These results are largely consistent with bulk RNA-seq analyses of P14 juvenile testes
429 (Supplemental Fig. S12), together indicating that MSCI is disrupted in *Atf7ip2*$^{-/-}$ pachytene
430 spermatocytes.
431
432 MSCI is initiated by the DDR pathway and maintained through active DDR signaling
433 (Ichijima et al. 2011; Abe et al. 2022). On the *Atf7ip2*$^{-/-}$ XY domain, γH2AX signals were
434 observed (Fig. 2), but H3K9me2/3 deposition was not established as the pachytene stage
435 progressed into the diplotene stage (Fig. 4). Indeed, in place of H3K9me2/3, we observed signals
436 for the active transcriptional mark H3K9ac (Supplemental Figure S4B). Thus, we suspect that

bioRxiv preprint doi: https://doi.org/10.1101/2023.09.30.560314; this version posted October 2, 2023. The copyright holder for this preprint (which was not certified by peer review) is the author/funder, who has granted bioRxiv a license to display the preprint in perpetuity. It is made available under aCC-BY-NC-ND 4.0 International license.

437 MSCI is initiated but not maintained in *Atf7ip2*$^{-/-}$ spermatocytes. To test this, we stained for
438 POLII in *Atf7ip2*$^{-/-}$ pachytene spermatocytes. In normal mid pachytene spermatocytes, we
439 observed the exclusion of POLII from XY domains in 100% of observed nuclei (n = 65,
440 Supplemental Fig. S11C), confirming the accurate detection of MSCI through POLII
441 immunostaining. However, in *Atf7ip2*$^{-/-}$ mid pachytene spermatocytes, we observed the exclusion
442 of POLII from XY chromatin in only 73.3% of nuclei (n = 105, Supplemental Fig. S11D); 26.7%
443 of *Atf7ip2*$^{-/-}$ nuclei saw the inclusion of POLII in XY domains (Supplemental Fig. S11E)—
444 evidence for defective MSCI. These results suggest that, in the absence of ATF7IP2, the
445 initiation of MSCI occurs, but MSCI fails to be maintained.
446
447 In terms of γH2AX signals on XY chromatin and the loss of H3K9me3 deposition, the
448 *Atf7ip2*$^{-/-}$ phenotype overlaps the reported phenotype for *Setdb1*-cKO mice (Hirota et al. 2018;
449 Cheng et al. 2021; Abe et al. 2022). To determine the relationship between *Atf7ip2* and *Setdb1*
450 mutations, we reanalyzed *Setdb1*-cKO RNA-seq data for pachytene spermatocytes (Hirota et al.
451 2018) (Supplemental Fig. S12). Although MSCI was disrupted, the massive downregulation of
452 autosomal genes was not observed in the *Setdb1*-cKO spermatocytes. Thus, we infer that
453 ATF7IP2's gene regulatory functions are broader in consequence than those of SETDB1.
454
455 To understand the mechanism through which ATF7IP2 regulates H3K9me3 deposition,
456 we produced and analyzed H3K9me3 CUT&RUN data from *Atf7ip2*$^{+/+}$ and *Atf7ip2*$^{-/-}$ pachytene
457 spermatocytes (Supplemental Fig. 10F). We found that H3K9me3 is largely dependent on
458 ATF7IP2, especially at the sites of Cluster II ATF7IP2-bound peaks (Fig. 7C; Cluster II peaks
459 were defined in Fig. 6B). ATF7IP2 and H3K9me3 signals frequently overlapped, with many

bioRxiv preprint doi: https://doi.org/10.1101/2023.09.30.560314; this version posted October 2, 2023. The copyright holder for this preprint (which was not certified by peer review) is the author/funder, who has granted bioRxiv a license to display the preprint in perpetuity. It is made available under aCC-BY-NC-ND 4.0 International license.

460 regions of H3K9me3 deposition centered on ATF7IP2 peaks (Fig. 7C). Notably, H3K9me3
461 deposition was completely absent or strongly diminished in the *Atf7ip2*$^{-/-}$ model, indicating
462 H3K9me3 enrichment is dependent on ATF7IP2 (Fig. 7C). As shown in a track view of the Y-
463 linked *Zfy1* locus, ATF7IP2-binding sites frequently align with, or are immediately adjacent to,
464 locations of ATF7IP2-dependent H3K9me3 (Fig. 7D). Conversely, there was no observed
465 H3K9me3 enrichment on ATF7IP2-dependent autosomal genes, as evidenced by loci such as
466 *Hspa2* (Fig. 7E). We conclude that ATF7IP2 directs H3K9me3 deposition while simultaneously
467 orchestrating meiotic gene activation on autosomes, much of which is independent of H3K9me3.
468

469 *ATF7IP2 fine-tunes the expression of transposable elements*

470 SETDB1-mediated H3K9me3 is a well-known suppressor of transposable elements (TEs)
471 (Matsui et al. 2010; Rowe et al. 2013). Therefore, we sought to examine TE expression using our
472 RNA-seq data in combination with a "best-match" TE annotation set (Sakashita et al. 2020),
473 which enables the detection of alignments uniquely mapped to TEs that are not exon-derived
474 (mRNA-derived). This strategy eliminates detection of TEs that are parts of mRNA, preventing
475 the conflation of mRNA and TE expression. In *Atf7ip2*$^{-/-}$ pachytene spermatocytes, three TE
476 types (IAPEy-int, RLTR10B2, MMERVK10C-int) were upregulated, while 115 types were
477 downregulated (Fig. 7F). ATF7IP2 bound these upregulated TEs, and H3K9me3 at these loci
478 was ATF7IP2-dependent (Fig. 7G). In wild-type spermatogenesis, TE expression undergoes
479 dynamic changes at the mitosis-to-meiosis transition, and a subset of TEs—specifically
480 endogenous retrovirus K (ERV) families that are also known as long-terminal repeats (LTRs)—
481 are activated as enhancers in meiosis (Sakashita et al. 2020). Notably, these meiotic enhancer
482 ERVs (RLTR10B2) are among the upregulated TEs (Fig. 7F). The meiotic enhancer ERVs are

bioRxiv preprint doi: https://doi.org/10.1101/2023.09.30.560314; this version posted October 2, 2023. The copyright holder for this preprint (which was not certified by peer review) is the author/funder, who has granted bioRxiv a license to display the preprint in perpetuity. It is made available under aCC-BY-NC-ND 4.0 International license.

active in wild-type pachytene spermatocytes and were further upregulated in *Atf7ip2*$^{-/-}$ cells. Thus, ATF7IP2 may fine-tune the activity of these TEs. In contrast, various TE types, particularly those enriched with LTRs and active in the pachytene stage, were downregulated in *Atf7ip2*$^{-/-}$ spermatocytes. In all, our study identifies distinct functions for ATF7IP2 in regulating protein-coding genes on autosomes and sex chromosomes, as well as in the regulation of TEs (Fig. 7H, I, J).

Discussion

Our study identifies ATF7IP2 as a counterpart to ATF7IP that is highly expressed in the male germline and directs SETDB1-mediated H3K9 methylation—a conclusion supported by two major observations. First, in wild-type meiosis, ATF7IP2, SETDB1, and H3K9me3 accumulate on autosomal PCH; in pachytene spermatocytes, all are enriched on the X-PCH, the site from which they spread through the diplotene XY domain. Second, in *Atf7ip2*$^{-/-}$ pachytene spermatocytes, SETDB1 was grossly delocalized, and H3K9me2/3 was not present on the XY chromatin in the late pachytene-to-diplotene stages. As might be expected, the *Atf7ip2*$^{-/-}$ meiotic phenotype overlaps to some extent the meiotic phenotype of *Setdb1*-cKO mice. Thus, our study reveals the molecular logic for the management of SETDB1 and H3K9me3 in meiosis, demonstrating the unique nature of meiotic heterochromatin and its distinct regulation with respect to autosomes and the sex chromosomes.

However, in the early pachytene stage, there is a phenotypic difference between *Atf7ip2*$^{-/-}$ and *Setdb1*-cKO mice with regards to H3K9me3 localization: H3K9me3, a SETDB1-dependent marker of XY chromatin (Hirota et al. 2018; Abe et al. 2022), is affected but not completely

bioRxiv preprint doi: https://doi.org/10.1101/2023.09.30.560314; this version posted October 2, 2023. The copyright holder for this preprint (which was not certified by peer review) is the author/funder, who has granted bioRxiv a license to display the preprint in perpetuity. It is made available under aCC-BY-NC-ND 4.0 International license.

506 absent from XY chromatin in *Atf7ip2*$^{-/-}$ mice. Thus, there may be an alternate regulator of
507 SETDB1 in early pachytene spermatocytes. In support of this possibility, *Setdb1*-cKO
508 spermatocytes evidenced more severe chromosome synapsis defects (Hirota et al. 2018; Cheng et
509 al. 2021; Abe et al. 2022) than *Atf7ip2*$^{-/-}$ spermatocytes. Nevertheless, the meiotic arrest
510 phenotype indicates that the ATF7IP2-dependent regulation of SETDB1 (likely through an
511 ATF7IP2-SETDB1 complex) and H3K9me3 becomes essential in the pachytene-to-diplotene
512 transition.
513
514 Our study also reveals novel aspects of the meiotic sex chromosomes. We propose that,
515 through the recruitment of SETDB1, ATF7IP2 functions as an effector that links DDR signaling
516 and SETDB1-mediated H3K9me3. The γH2AX-binding partner MDC1 is necessary for the
517 recruitment of ATF7IP2 to X-PCH (Fig. 4G). A previous study proposed that TRIM28
518 (KAP1)—a SETDB1 partner in ERV suppression—links the DDR and SETDB1 on the meiotic
519 sex chromosomes (Hirota et al. 2018). However, we did not observe TRIM28 enrichment on XY,
520 and so we question TRIM28's status as a linker. Furthermore, it was reported that young *Trim28*
521 mutant mice are initially fertile and only become sterile with age (Tan et al. 2020), indicating
522 that TRIM28 is not essential for MSCI.
523
524 We find that the establishment of H3K9me2/3 on diplotene XY chromatin is ATF7IP2-
525 dependent. Given the extensive histone replacement that occurs in MSCI (H3.1/H3.2 to H3.3)
526 (van der Heijden et al. 2007), H3K9me2/3 deposition is likely to take place on "fresh" H3.3 in a
527 process that is also ATF7IP2-dependent. In the latter stages of spermatogenesis, H3K9me2/3 is a
528 persistent mark on the sex chromosomes, from MSCI to postmitotic silencing (Namekawa et al.

bioRxiv preprint doi: https://doi.org/10.1101/2023.09.30.560314; this version posted October 2, 2023. The copyright holder for this preprint (which was not certified by peer review) is the author/funder, who has granted bioRxiv a license to display the preprint in perpetuity. It is made available under aCC-BY-NC-ND 4.0 International license.

529 2007); thus, the ATF7IP2-dependent mechanisms described here could be driving heritable
530 epigenetic states through meiotic divisions.
531
532 Unexpectedly, our study demonstrates that ATF7IP2 is required for global gene
533 regulation in pachytene spermatocytes. In mid pachytene spermatocytes, a burst of gene
534 activation takes place, and this is driven by the transcription factor A-MYB (MYBL1) through
535 the activation of meiotic enhancers (Bolcun-Filas et al. 2011; Maezawa et al. 2020). Thus, there
536 is an intriguing possibility that such meiosis-specific transcription requires ATF7IP2.
537 Importantly, ATF7IP2 is present at thousands of autosomal promoters, where H3K9me3 is
538 notably absent. Thus, ATF7IP2 could regulate transcriptional mechanisms independent of
539 H3K9me3. Intriguingly, ATF7, an ATF7IP2-interacting protein, also accumulates on a wide
540 range of autosomal promoters in testicular germ cells, mediating epigenetic inheritance through
541 the regulation of H3K9me2 (Yoshida et al. 2020). In future studies, a key goal will be to
542 determine the mechanistic relationship between ATF7IP2 and ATF7 in the context of meiotic
543 gene regulation. While ATF7IP2's localization on the sex chromosomes requires MDC1, it is
544 unknown what regulates its recruitment to autosomes—although one possibility is ATM-
545 dependent DDR signaling. Furthermore, it is unknown what coordinates ATF7IP2's distinct
546 autosomal and XY functions.
547
548 Finally, we show that ATF7IP2 fine-tunes the expression of retrotransposon-derived loci
549 in male germ cells, a function that coincides with SETDB1's role in TE silencing. In *Atf7ip2*$^{-/-}$
550 spermatocytes, we observed the upregulated expression of immune genes, a phenomenon akin to
551 SETDB1-mediated immune escape in tumorigenesis (Griffin et al. 2021). In tumor cells, the

bioRxiv preprint doi: https://doi.org/10.1101/2023.09.30.560314; this version posted October 2, 2023. The copyright holder for this preprint (which was not certified by peer review) is the author/funder, who has granted bioRxiv a license to display the preprint in perpetuity. It is made available under aCC-BY-NC-ND 4.0 International license.

552 depletion of SETDB1 facilitates the expression of immune genes, thereby driving the intrinsic
553 immunogenicity of tumors. Also in tumor cells, SETDB1 works together with the HUSH
554 complex—itself functionally linked to ATF7IP (Timms et al. 2016)—to suppress large domains
555 of the genome enriched for rapidly evolved TEs (Griffin et al. 2021). Notably, a large number of
556 the germline genes activated in pachytene spermatocytes are rapidly evolved (Soumillon et al.
557 2013), as are the meiotic ERV enhancer loci that drive germline gene expression (Sakashita et al.
558 2020). In wild-type spermatocytes, these loci are associated with broad domains of H3K9me3.
559 Furthermore, like many tumor cells, testicular germ cells are immunoprivileged, found beyond
560 the blood-testes barrier. Given the similarities between germ and tumor cells, it is possible that
561 ATF7IP2-directed SETDB1 mechanisms, which regulate MSCI and TEs, drive the quick-paced
562 evolution of the germline genome. It may be that this work establishes a foundation to
563 understand the mechanisms behind germline evolution in mammals.
564
565 A recent study reported another *Atf7ip2* mutant mouse line (Shao et al. 2023), and
566 although the mouse phenotypes detailed in the two studies were largely consistent, we did not
567 observe the reported difference in XY obligatory crossover (Shao et al. 2023). This could be due
568 to an *Atf7ip2* mutational difference in the mouse lines. Further investigations are warranted to
569 clarify the role of ATF7IP2 in male meiosis.
570

571 **Materials and Methods**

572

573 **Animals**

bioRxiv preprint doi: https://doi.org/10.1101/2023.09.30.560314; this version posted October 2, 2023. The copyright holder for this preprint (which was not certified by peer review) is the author/funder, who has granted bioRxiv a license to display the preprint in perpetuity. It is made available under aCC-BY-NC-ND 4.0 International license.

All mice were handled according to the guidelines of the Institutional Animal Care and Use Committee (IACUC: protocol no. IACUC2018-0040 and 21931) at Cincinnati Children's Hospital Medical Center and the University of California, Davis.

Generation of *Atf7ip2*$^{-/-}$ mice

Atf7ip2$^{-/-}$ mice were generated using a sgRNA (target sequence: TTCATGTCTACTCTTGCACT) that was selected according to location and the on- and off-target scores from the web tool CRISPOR (Haeussler et al. 2016).

Preparation of meiotic chromosome spreads

Meiotic chromosome spread preparation, immunostaining, and data analysis were performed as described (Alavattam et al. 2018). Histology and immunostaining were performed as described (Abe et al. 2022).

Isolation of pachytene spermatocytes

Isolation of pachytene spermatocytes using Fluorescence-activated cell sorting (FACS) was performed using SH800S (SONY), with Vybrant DyeCycle Violet Stain (DCV) (Invitrogen, V35003) stained testicular single-cell suspensions prepared as described previously (Yeh et al. 2021).

Next-generation sequencing analysis

Library generation and data analyses for bulk RNA-seq, CUT&Tag, CUT&RUN, and scRNA-seq are described in the Supplemental Material.

bioRxiv preprint doi: https://doi.org/10.1101/2023.09.30.560314; this version posted October 2, 2023. The copyright holder for this preprint (which was not certified by peer review) is the author/funder, who has granted bioRxiv a license to display the preprint in perpetuity. It is made available under aCC-BY-NC-ND 4.0 International license.

Other detailed experimental procedures are described in the Supplemental Material.

Data Availability

RNA-seq data and CUT&RUN/Tag datasets were deposited in the Gene Expression Omnibus (accession: GSE244088). Testes bulk RNA-seq data reported in this paper were deposited in the Gene Expression Omnibus (accession: GSE223742). Single-cell RNA-seq data are available at DDBJ Sequence Read Archive (DRA) under the BioProject accession: PRJDB16643.

Author contributions

K.G.A., J.M.E., M.H., R.S., K.-I.I., and S.H.N. designed the study. K.G.A., J.M.E., M.H., A.R.K., H.A., Y.K., Y.-H.Y., and J.K. performed experiments. K.G.A., J.M.E., M.H, A.R.K., H.A., M.H, Y.K. analyzed the mouse phenotypes. J.M.E., M.H isolated germ cells and performed scRNA-seq experiments. M.H performed bulk RNA-seq, CUT&Tag, CUT&RUN experiments. R.S. analyzed the scRNA-seq data. K.G.A., J.M.E., M.H, R.S., Y.M., K.O., S.Y., K.-I.I., and S.H.N. designed and interpreted the computational analyses. Y.-C.H. generated the *Atf7ip2*-/- mouse line. K.G.A., J.M.E., M.H., R.S., P.R.A, K.-I.I., and S.H.N. interpreted the results and wrote the manuscript with critical feedback from all other authors. S.H.N. supervised the project.

Acknowledgments

We thank Yoshinori Watanabe, Hiroki Shibuya, Akihiro Morimoto, and Shohei Yamamoto for their contributions to the early stage of this investigation; members of the Namekawa laboratory

bioRxiv preprint doi: https://doi.org/10.1101/2023.09.30.560314; this version posted October 2, 2023. The copyright holder for this preprint (which was not certified by peer review) is the author/funder, who has granted bioRxiv a license to display the preprint in perpetuity. It is made available under aCC-BY-NC-ND 4.0 International license.

for discussion and helpful comments regarding this manuscript; So Maezawa and Masashi Yukawa for the initial RNA-seq analysis; Neil Hunter and Richard M. Schultz for discussion; Yasuhiro Fujiwara and Yuki Okada for aiding in the transfer of the anti-ATF7IP2 antibody; the Transgenic Animal and Genome Editing Core at CCHMC for generation of the *Atf7ip2*$^{-/-}$ mouse model; Yoichi Shinkai for providing the *Setdb1* floxed mouse line, Junjie Chen for providing the *Mdc1*-KO mice, and Mary Ann Handel for providing the anti-H1T antibody. Funding sources: NIH Training Program in Molecular and Cellular Biology T32GM007377 and Ford Foundation Predoctoral Fellowship to J.E.; R01 GM134731 to P.R.A.; KAKENHI #19H05743, #23H00379 and AMED PRIME #23gm6310021h0003, the program of the Research for High Depth Omics, IMEG, Kumamoto University to K.I.I.; UC Davis startup fund, and NIH R01 GM098605, R35 GM141085, and GM141085 diversity supplement to S.H.N.

bioRxiv preprint doi: https://doi.org/10.1101/2023.09.30.560314; this version posted October 2, 2023. The copyright holder for this preprint (which was not certified by peer review) is the author/funder, who has granted bioRxiv a license to display the preprint in perpetuity. It is made available under aCC-BY-NC-ND 4.0 International license.

633 **Figure legends**

634 **Figure 1. ATF7IP2 is highly expressed in male meiosis and accumulates on**
635 **heterochromatin.**

636 **(A, C)** Heatmaps showing bulk RNA-seq gene expression levels across a male-germline time
637 course for *Atf7ip2* and related genes. PGC: Primordial germ cells, ProSG: prospermatogonia,
638 SG: spermatogonia, PS: pachytene spermatocytes, RS: round spermatids. Original data are from
639 (Seisenberger et al. 2012; Hasegawa et al. 2015; Maezawa et al. 2018b) for (**A**) and (Ishiguro et
640 al. 2020) for (**C**)

641 **(B)** Track views for MEIOSIN (preleptotene-enriched testes), STRA8 (preleptotene-enriched
642 testes), and RNA polymerase II (POLII; postnatal day (P) 10.5 testes) ChIP-seq data, and CAGE
643 (P10.5 testes). Numbers in brackets: ranges of normalized coverage.

644 **(D)** Schematic: chromosome behavior in meiotic prophase I of male *Mus musculus*. Darker
645 green: autosomes; lighter green: sex chromosomes.

646 **(E)** Meiotic chromosome spreads stained with DAPI and antibodies raised against ATF7IP2,
647 SYCP3, and H1T; spreads represent stages of meiotic prophase I. Insets: H1T immunostaining;
648 H1T is a nuclear marker that appears in mid pachytene nuclei and persists into haploid
649 spermatids. SYCP3 is a marker of meiotic chromosome axes. Dashed squares are magnified in
650 panel **F**. Scale bars: 5 µm.

651 **(F)** Schematic: sex chromosome configuration in male meiosis. Right: magnified images of sex
652 chromosomes from panel **E**. Scale bars: 5 µm.

653

654 **Figure 2. ATF7IP2 is required for male fertility.**

655 **(A)** Schematic: mouse *Atf7ip2* gene and the location of the CRISPR-mediated deletion.

bioRxiv preprint doi: https://doi.org/10.1101/2023.09.30.560314; this version posted October 2, 2023. The copyright holder for this preprint (which was not certified by peer review) is the author/funder, who has granted bioRxiv a license to display the preprint in perpetuity. It is made available under aCC-BY-NC-ND 4.0 International license.

656 **(B)** Schematic: mouse ATF7IP2 and ATF7IP proteins, and their functional domains.

657 **(C)** *Atf7ip2*$^{+/+}$ and *Atf7ip2*$^{-/-}$ males, and their testes, at postnatal day 66 (P66). Scale bars: 10 mm.

658 **(D)** Cumulative numbers of pups sired with *Atf7ip2+/-* and *Atf7ip2-/-* males.

659 **(E)** Testis weights for *Atf7ip2*$^{-/-}$ males and littermate controls (*Atf7ip2* ctrl: *Atf7ip2*$^{+/+}$ and

660 *Atf7ip2*$^{+/-}$). Numbers of independent mice analyzed are shown in parentheses. P-values are from

661 pairwise t-tests adjusted with Benjamini-Hochberg post-hoc tests: *** < 0.001. Data are

662 presented as mean ± SEM.

663 **(F)** Testis sections from *Atf7ip2*$^{+/+}$ and *Atf7ip2*$^{-/-}$ mice at 4 months of age stained with DAPI and

664 antibodies raised against ATF7IP2, γH2AX (a marker of the DNA damage response), and H1T

665 (a marker of germ cells in mid pachytene and subsequent stages). Scale bars: 100 µm.

666

667 **Figure 3. DDR and chromosome synapsis are mildly impaired in *Atf7ip2*$^{-/-}$ spermatocytes.**

668 **(A)** *Atf7ip2*$^{+/+}$ and *Atf7ip2*$^{-/-}$ spermatocyte chromosome spreads stained with antibodies raised

669 against SYCP3 and γH2AX. γH2AX accumulation patterns are one of three classifications

670 described in panel **C**. Scale bars: 10 µm.

671 **(B)** Meiotic prophase I stage populations quantified as mean ± SEM for three independent

672 littermate pairs. Numbers of analyzed nuclei are indicated. Data are from five independent

673 littermate pairs at P44, P56, P66, P66, and P69. P-values are from unpaired two-tailed t-tests: * <

674 0.05, ** < 0.01.

675 **(C)** Stage-wise proportions of γH2AX accumulation patterns for three independent littermate

676 pairs. Patterns are classified with three criteria (see top). P-values are from Fisher's exact tests:

677 **** < 0.0001.

bioRxiv preprint doi: https://doi.org/10.1101/2023.09.30.560314; this version posted October 2, 2023. The copyright holder for this preprint (which was not certified by peer review) is the author/funder, who has granted bioRxiv a license to display the preprint in perpetuity. It is made available under aCC-BY-NC-ND 4.0 International license.

(D) Chromosome spreads stained with antibodies raised against SYCP3 and MLH1. Arrowheads indicate MLH1 foci. Dot plot (top): distributions of MLH1 counts from three independent littermate pairs. Dot plot (bottom): proportions of MLH1 focus-associated XY pseudoautosomal regions (PARs) from three independent littermate pairs. Numbers of analyzed nuclei are indicated. Data are from three independent littermate pairs at P108, P115, P122. Bars represent means. P-values are from unpaired t-tests.

(E, F) Chromosome spreads stained with antibodies raised against SYCP3 (a marker of all chromosome axes) and SYCP1 (a marker of only synapsed axes). Scale bars: 10 µm (**E**), 5 µm (**F**). Bar plots: proportions of pachytene nuclei with normal synapsis of autosomes (**E**) and sex chromosomes (**F**). Data are from four independent littermate pairs at P44, P66, P66, and P69, and presented as mean ± SEM. P-values are from unpaired t-tests: * < 0.05, ** < 0.01.

Figure 4: ATF7IP2 is required for H3K9 methylation on the sex chromosomes during male meiosis.

(A) *Atf7ip2*$^{+/+}$ and *Atf7ip2*$^{-/-}$ spermatocyte chromosome spreads stained with antibodies raised against H3K9me3 and SYCP3 (a marker of chromosome axes, both synapsed and unsynapsed). Dashed circles indicate the sex chromosomes. Scale bars: 10 µm.

(B) H3K9me3 accumulation patterns on the sex chromosomes of *Atf7ip2*$^{+/+}$ and *Atf7ip2*$^{-/-}$ early pachytene spermatocytes. Patterns are classified with four criteria (see right). Three independent experiments. P-values are from Fisher's exact tests: **** < 0.0001. Scale bars: 10 µm.

(C) Quantification of mid pachytene, late pachytene, and diplotene spermatocytes with H3K9me3 signals on the sex chromosomes. Three independent experiments. P-values are from Fisher's exact tests: * < 0.05, *** < 0.001, **** < 0.0001.

bioRxiv preprint doi: https://doi.org/10.1101/2023.09.30.560314; this version posted October 2, 2023. The copyright holder for this preprint (which was not certified by peer review) is the author/funder, who has granted bioRxiv a license to display the preprint in perpetuity. It is made available under aCC-BY-NC-ND 4.0 International license.

(D) Chromosome spreads stained with antibodies raised against H3K9me2 and SYCP3.

(E) Quantification of diplotene spermatocytes with H3K9me2 signals on the sex chromosomes. Three independent experiments. P-values are from Fisher's exact tests, **** < 0.0001.

(F) Chromosome spreads stained with antibodies raised against SETDB1 and SYCP3. Dashed squares are magnified in the panels to the right. Scale bars: 10 μm.

(G) *Mdc1*$^{+/+}$ and *Mdc1*$^{-/-}$ spermatocyte chromosome spreads stained with antibodies raised against ATF7IP2 and SYCP3. Scale bars: 10 μm.

(H) Summary of the γH2AX/MDC1-ATF7IP2-SETDB1 pathway on X-PCH.

(I) Schematic: establishment of H3K9me3 on the sex chromosomes in normal mid pachytene-to-diplotene spermatocytes.

Figure 5. scRNA-seq analyses of *Atf7ip2*$^{+/+}$ and *Atf7ip2*$^{-/-}$ spermatogenic germ cells

(A) UMAP representations of scRNA-seq transcriptome profiles for germ cells from *Atf7ip2*$^{+/+}$ testes (left: P15), *Atf7ip2*$^{-/-}$ testes (middle: P15), and both *Atf7ip2*$^{+/+}$ and *Atf7ip2*$^{-/-}$ testes (right). Gray arrow: inferred developmental trajectory.

(B) Clustering of UMAP-projected scRNA-seq transcriptome profiles for *Atf7ip2*$^{+/+}$ and *Atf7ip2*$^{-/-}$ germ cells based on gene expression patterns.

(C) Bar graph showing the proportions of *Atf7ip2*$^{+/+}$ and *Atf7ip2*$^{-/-}$ germ cells among the clusters.

(D) UMAP representations showing expression patterns for key developmental marker genes in spermatogenic cells. Genes include *Gfra1*, which represent undifferentiated spermatogonia; *Stra8*, differentiating spermatogonia; *Meiosin*, preleptotene spermatocytes; and *Prdm9*, early meiotic prophase spermatocytes. P-values are from Wilcoxon rank sum tests: n.s., not significant; * < 0.05.

bioRxiv preprint doi: https://doi.org/10.1101/2023.09.30.560314; this version posted October 2, 2023. The copyright holder for this preprint (which was not certified by peer review) is the author/funder, who has granted bioRxiv a license to display the preprint in perpetuity. It is made available under aCC-BY-NC-ND 4.0 International license.

724 **(E)** Expression patterns for *Atf7ip2* and *Atf7ip* upon the UMAP.

725 **(F)** Expression levels for autosomal genes. P-values are from Wilcoxon rank sum tests: * < 0.05,

726 ** < 0.01, *** < 0.001.

727 **(G)** Expression levels for X chromosomal genes (top) and Y chromosomal genes (bottom). P-

728 values are from Wilcoxon rank sum tests: * < 0.05, ** < 0.01, *** < 0.001.

729 **(H)** Summary of *Atf7ip2*$^{-/-}$ phenotypes in spermatogenic germ cells. Subtype clusters are ordered

730 by inferred developmental progression. Key cell types and events in *Atf7ip2*$^{+/+}$ and *Atf7ip2*$^{-/-}$

731 spermatogenesis are shown.

732

733 **Figure 6. ATF7IP2-binding sites in pachytene spermatocytes.**

734 **(A)** Numbers and genomic distribution of ATF7IP2 CUT&Tag peaks in wild-type pachytene

735 spermatocytes.

736 **(B)** Two-step clustering analysis of ATF7IP2 CUT&Tag peaks and H3K9me3 and H3K4me3

737 enriched-regions. Average tag density profiles (top) and heatmaps for each cluster (bottom).

738 **(C)** Chromosomal distribution of ATF7IP2 peak clusters.

739 **(D)** Genomic distribution of ATF7IP2 peak clusters.

740 **(E)** Expression levels of ATF7IP2-bound autosomal genes in scRNA-seq. P-values are from

741 Wilcoxon rank sum tests: * < 0.05, ** < 0.01.

742 **(F)** Expression levels for ATF7IP2-bound sex chromosomal genes in scRNA-seq. P-values are

743 from Wilcoxon rank sum tests: * < 0.05, ** < 0.01, *** < 0.001

744

745 **Figure 7. ATF7IP2 directs meiotic gene regulation and regulates TEs.**

bioRxiv preprint doi: https://doi.org/10.1101/2023.09.30.560314; this version posted October 2, 2023. The copyright holder for this preprint (which was not certified by peer review) is the author/funder, who has granted bioRxiv a license to display the preprint in perpetuity. It is made available under aCC-BY-NC-ND 4.0 International license.

(**A**) Comparison of *Atf7ip2*$^{+/+}$ and *Atf7ip2*$^{-/-}$ pachytene spermatocyte transcriptomes. Autosomal, X, and Y genes were analyzed separately. Two independent biological replicates were examined. All genes with adjusted p-values (Benjamini-Hochberg method) are plotted. Differentially expressed genes (DEGs: $\log_2$ fold change ≥ 2, adjusted p-value ≤ 0.05) are colored (red: upregulated in *Atf7ip2*$^{-/-}$ testes; blue: downregulated in *Atf7ip2*$^{-/-}$ testes), and numbers are shown.

(**B**) ATF7IP2 CUT&Tag enrichment at DEG TSSs ± 2 kb in pachytene spermatocytes isolated from *Atf7ip2*$^{-/-}$ mice. Average tag density profiles (top) and heatmaps for each cluster (bottom).

(**C**) ATF7IP2 CUT&Tag and H3K9me3 CUT&RUN enrichment in Clusters I–III (defined in Fig. 6B). Average tag density profiles (top) and heatmaps for each cluster (bottom).

(**D, E**) Track views of the *Zfy1* locus (an upregulated Y-linked locus) and the *Hspa2* locus (a downregulated autosomal locus).

(**F**) Comparison of *Atf7ip2*$^{+/+}$ and *Atf7ip2*$^{-/-}$ pachytene spermatocyte transposable element (TE) expression. All TE types are plotted. Differentially expressed TE types (DEGs: $\log_2$ fold change > 2, adjusted p-value < 0.05) are colored (red: upregulated in *Atf7ip2*$^{-/-}$; blue: downregulated in *Atf7ip2*$^{-/-}$), and numbers are shown.

(**G**) Track view of the ATF7IP2-targeted TEs RLTR10B2 and MMERVK10C-int.

(**H**) Summary and model of the function of ATF7IP2 on X-PCH.

(**I**) Summary and model of the function of ATF7IP2 in TE regulation.

(**J**) Summary and model of the function of ATF7IP2 in gene expression regulation.

bioRxiv preprint doi: https://doi.org/10.1101/2023.09.30.560314; this version posted October 2, 2023. The copyright holder for this preprint (which was not certified by peer review) is the author/funder, who has granted bioRxiv a license to display the preprint in perpetuity. It is made available under aCC-BY-NC-ND 4.0 International license.

768 **References**

769 Abe H, Alavattam KG, Kato Y, Castrillon DH, Pang Q, Andreassen PR, Namekawa SH. 2018.
770 CHEK1 coordinates DNA damage signaling and meiotic progression in the male
771 germline of mice. *Hum Mol Genet* **27**: 1136-1149.

772 Abe H, Yeh YH, Munakata Y, Ishiguro KI, Andreassen PR, Namekawa SH. 2022. Active DNA
773 damage response signaling initiates and maintains meiotic sex chromosome inactivation.
774 *Nat Commun* **13**: 7212.

775 Alavattam KG, Abe H, Sakashita A, Namekawa SH. 2018. Chromosome Spread Analyses of
776 Meiotic Sex Chromosome Inactivation. *Methods Mol Biol* **1861**: 113-129.

777 Alavattam KG, Kato Y, Sin HS, Maezawa S, Kowalski IJ, Zhang F, Pang Q, Andreassen PR,
778 Namekawa SH. 2016. Elucidation of the Fanconi Anemia Protein Network in Meiosis
779 and Its Function in the Regulation of Histone Modifications. *Cell Rep* **17**: 1141-1157.

780 Alavattam KG, Maezawa S, Andreassen PR, Namekawa SH. 2021. Meiotic sex chromosome
781 inactivation and the XY body: a phase separation hypothesis. *Cell Mol Life Sci* **79**: 18.

782 Ashburner M, Ball CA, Blake JA, Botstein D, Butler H, Cherry JM, Davis AP, Dolinski K,
783 Dwight SS, Eppig JT et al. 2000. Gene ontology: tool for the unification of biology. The
784 Gene Ontology Consortium. *Nat Genet* **25**: 25-29.

785 Becker JS, Nicetto D, Zaret KS. 2016. H3K9me3-Dependent Heterochromatin: Barrier to Cell
786 Fate Changes. *Trends Genet* **32**: 29-41.

787 Bellani MA, Romanienko PJ, Cairatti DA, Camerini-Otero RD. 2005. SPO11 is required for sex-
788 body formation, and Spo11 heterozygosity rescues the prophase arrest of Atm-/-
789 spermatocytes. *J Cell Sci* **118**: 3233-3245.

bioRxiv preprint doi: https://doi.org/10.1101/2023.09.30.560314; this version posted October 2, 2023. The copyright holder for this preprint (which was not certified by peer review) is the author/funder, who has granted bioRxiv a license to display the preprint in perpetuity. It is made available under aCC-BY-NC-ND 4.0 International license.

790 Berrios S. 2017. Nuclear Architecture of Mouse Spermatocytes: Chromosome Topology,
791 Heterochromatin, and Nucleolus. *Cytogenet Genome Res* **151**: 61-71.
792 Bilodeau S, Kagey MH, Frampton GM, Rahl PB, Young RA. 2009. SetDB1 contributes to
793 repression of genes encoding developmental regulators and maintenance of ES cell state.
794 *Genes Dev* **23**: 2484-2489.
795 Bolcun-Filas E, Bannister LA, Barash A, Schimenti KJ, Hartford SA, Eppig JJ, Handel MA,
796 Shen L, Schimenti JC. 2011. A-MYB (MYBL1) transcription factor is a master regulator
797 of male meiosis. *Development* **138**: 3319-3330.
798 Broering TJ, Alavattam KG, Sadreyev RI, Ichijima Y, Kato Y, Hasegawa K, Camerini-Otero
799 RD, Lee JT, Andreassen PR, Namekawa SH. 2014. BRCA1 establishes DNA damage
800 signaling and pericentric heterochromatin of the X chromosome in male meiosis. *J Cell*
801 *Biol* **205**: 663-675.
802 Cheng EC, Hsieh CL, Liu N, Wang J, Zhong M, Chen T, Li E, Lin H. 2021. The Essential
803 Function of SETDB1 in Homologous Chromosome Pairing and Synapsis during Meiosis.
804 *Cell Rep* **34**: 108575.
805 Fernandez-Capetillo O, Mahadevaiah SK, Celeste A, Romanienko PJ, Camerini-Otero RD,
806 Bonner WM, Manova K, Burgoyne P, Nussenzweig A. 2003. H2AX is required for
807 chromatin remodeling and inactivation of sex chromosomes in male mouse meiosis. *Dev*
808 *Cell* **4**: 497-508.
809 Griffin GK, Wu J, Iracheta-Vellve A, Patti JC, Hsu J, Davis T, Dele-Oni D, Du PP, Halawi AG,
810 Ishizuka JJ et al. 2021. Epigenetic silencing by SETDB1 suppresses tumour intrinsic
811 immunogenicity. *Nature* **595**: 309-314.

bioRxiv preprint doi: https://doi.org/10.1101/2023.09.30.560314; this version posted October 2, 2023. The copyright holder for this preprint (which was not certified by peer review) is the author/funder, who has granted bioRxiv a license to display the preprint in perpetuity. It is made available under aCC-BY-NC-ND 4.0 International license.

Haeussler M, Schönig K, Eckert H, Eschstruth A, Mianné J, Renaud JB, Schneider-Maunoury S, Shkumatava A, Teboul L, Kent J et al. 2016. Evaluation of off-target and on-target scoring algorithms and integration into the guide RNA selection tool CRISPOR. *Genome Biol* **17**: 148.

Hasegawa K, Sin HS, Maezawa S, Broering TJ, Kartashov AV, Alavattam KG, Ichijima Y, Zhang F, Bacon WC, Greis KD et al. 2015. SCML2 establishes the male germline epigenome through regulation of histone H2A ubiquitination. *Dev Cell* **32**: 574-588.

Hirota T, Blakeley P, Sangrithi MN, Mahadevaiah SK, Encheva V, Snijders AP, ElInati E, Ojarikre OA, de Rooij DG, Niakan KK et al. 2018. SETDB1 Links the Meiotic DNA Damage Response to Sex Chromosome Silencing in Mice. *Dev Cell* **47**: 645-659.e646.

Ichijima Y, Ichijima M, Lou Z, Nussenzweig A, Camerini-Otero RD, Chen J, Andreassen PR, Namekawa SH. 2011. MDC1 directs chromosome-wide silencing of the sex chromosomes in male germ cells. *Genes Dev* **25**: 959-971.

Ichimura T, Watanabe S, Sakamoto Y, Aoto T, Fujita N, Nakao M. 2005. Transcriptional repression and heterochromatin formation by MBD1 and MCAF/AM family proteins. *J Biol Chem* **280**: 13928-13935.

Inselman A, Eaker S, Handel MA. 2003. Temporal expression of cell cycle-related proteins during spermatogenesis: establishing a timeline for onset of the meiotic divisions. *Cytogenet Genome Res* **103**: 277-284.

Ishiguro KI, Matsuura K, Tani N, Takeda N, Usuki S, Yamane M, Sugimoto M, Fujimura S, Hosokawa M, Chuma S et al. 2020. MEIOSIN Directs the Switch from Mitosis to Meiosis in Mammalian Germ Cells. *Dev Cell* **52**: 429-445.e410.

bioRxiv preprint doi: https://doi.org/10.1101/2023.09.30.560314; this version posted October 2, 2023. The copyright holder for this preprint (which was not certified by peer review) is the author/funder, who has granted bioRxiv a license to display the preprint in perpetuity. It is made available under aCC-BY-NC-ND 4.0 International license.

Kojima ML, de Rooij DG, Page DC. 2019. Amplification of a broad transcriptional program by a common factor triggers the meiotic cell cycle in mice. *Elife* **8**.

Li XZ, Roy CK, Dong X, Bolcun-Filas E, Wang J, Han BW, Xu J, Moore MJ, Schimenti JC, Weng Z et al. 2013. An ancient transcription factor initiates the burst of piRNA production during early meiosis in mouse testes. *Mol Cell* **50**: 67-81.

Liu S, Brind'Amour J, Karimi MM, Shirane K, Bogutz A, Lefebvre L, Sasaki H, Shinkai Y, Lorincz MC. 2014. Setdb1 is required for germline development and silencing of H3K9me3-marked endogenous retroviruses in primordial germ cells. *Genes Dev* **28**: 2041-2055.

Maezawa S, Hasegawa K, Alavattam KG, Funakoshi M, Sato T, Barski A, Namekawa SH. 2018a. SCML2 promotes heterochromatin organization in late spermatogenesis. *J Cell Sci* **131**.

Maezawa S, Hasegawa K, Yukawa M, Kubo N, Sakashita A, Alavattam KG, Sin HS, Kartashov AV, Sasaki H, Barski A et al. 2018b. Polycomb protein SCML2 facilitates H3K27me3 to establish bivalent domains in the male germline. *Proc Natl Acad Sci U S A* **115**: 4957-4962.

Maezawa S, Sakashita A, Yukawa M, Chen X, Takahashi K, Alavattam KG, Nakata I, Weirauch MT, Barski A, Namekawa SH. 2020. Super-enhancer switching drives a burst in gene expression at the mitosis-to-meiosis transition. *Nat Struct Mol Biol* **27**: 978-988.

Mahadevaiah SK, Turner JM, Baudat F, Rogakou EP, de Boer P, Blanco-Rodríguez J, Jasin M, Keeney S, Bonner WM, Burgoyne PS. 2001. Recombinational DNA double-strand breaks in mice precede synapsis. *Nat Genet* **27**: 271-276.

bioRxiv preprint doi: https://doi.org/10.1101/2023.09.30.560314; this version posted October 2, 2023. The copyright holder for this preprint (which was not certified by peer review) is the author/funder, who has granted bioRxiv a license to display the preprint in perpetuity. It is made available under aCC-BY-NC-ND 4.0 International license.

856 Matsui T, Leung D, Miyashita H, Maksakova IA, Miyachi H, Kimura H, Tachibana M, Lorincz
857 MC, Shinkai Y. 2010. Proviral silencing in embryonic stem cells requires the histone
858 methyltransferase ESET. *Nature* **464**: 927-931.
859 Mochizuki K, Tando Y, Sekinaka T, Otsuka K, Hayashi Y, Kobayashi H, Kamio A, Ito-
860 Matsuoka Y, Takehara A, Kono T et al. 2018. SETDB1 is essential for mouse primordial
861 germ cell fate determination by ensuring BMP signaling. *Development* **145**.
862 Namekawa SH, VandeBerg JL, McCarrey JR, Lee JT. 2007. Sex chromosome silencing in the
863 marsupial male germ line. *Proc Natl Acad Sci U S A* **104**: 9730-9735.
864 Nicetto D, Zaret KS. 2019. Role of H3K9me3 heterochromatin in cell identity establishment and
865 maintenance. *Curr Opin Genet Dev* **55**: 1-10.
866 Peters AH, O'Carroll D, Scherthan H, Mechtler K, Sauer S, Schöfer C, Weipoltshammer K,
867 Pagani M, Lachner M, Kohlmaier A et al. 2001. Loss of the Suv39h histone
868 methyltransferases impairs mammalian heterochromatin and genome stability. *Cell* **107**:
869 323-337.
870 Rowe HM, Friedli M, Offner S, Verp S, Mesnard D, Marquis J, Aktas T, Trono D. 2013. De
871 novo DNA methylation of endogenous retroviruses is shaped by KRAB-ZFPs/KAP1 and
872 ESET. *Development* **140**: 519-529.
873 Royo H, Prosser H, Ruzankina Y, Mahadevaiah SK, Cloutier JM, Baumann M, Fukuda T, Höög
874 C, Tóth A, de Rooij DG et al. 2013. ATR acts stage specifically to regulate multiple
875 aspects of mammalian meiotic silencing. *Genes Dev* **27**: 1484-1494.
876 Sakashita A, Maezawa S, Takahashi K, Alavattam KG, Yukawa M, Hu YC, Kojima S, Parrish
877 NF, Barski A, Pavlicev M et al. 2020. Endogenous retroviruses drive species-specific
878 germline transcriptomes in mammals. *Nat Struct Mol Biol* **27**: 967-977.

bioRxiv preprint doi: https://doi.org/10.1101/2023.09.30.560314; this version posted October 2, 2023. The copyright holder for this preprint (which was not certified by peer review) is the author/funder, who has granted bioRxiv a license to display the preprint in perpetuity. It is made available under aCC-BY-NC-ND 4.0 International license.

879 Saksouk N, Simboeck E, Déjardin J. 2015. Constitutive heterochromatin formation and
880 transcription in mammals. *Epigenetics Chromatin* **8**: 3.
881 Scherthan H, Schöfisch K, Dell T, Illner D. 2014. Contrasting behavior of heterochromatic and
882 euchromatic chromosome portions and pericentric genome separation in pre-bouquet
883 spermatocytes of hybrid mice. *Chromosoma* **123**: 609-624.
884 Seisenberger S, Andrews S, Krueger F, Arand J, Walter J, Santos F, Popp C, Thienpont B, Dean
885 W, Reik W. 2012. The dynamics of genome-wide DNA methylation reprogramming in
886 mouse primordial germ cells. *Mol Cell* **48**: 849-862.
887 Shao Q, Zhang Y, Liu Y, Shang Y, Li S, Liu L, Wang G, Zhou X, Wang P, Gao J et al. 2023.
888 ATF7IP2, a meiosis-specific partner of SETDB1, is required for proper chromosome
889 remodeling and crossover formation during spermatogenesis. *Cell Rep* **42**: 112953.
890 Soumillon M, Necsulea A, Weier M, Brawand D, Zhang X, Gu H, Barthès P, Kokkinaki M, Nef
891 S, Gnirke A et al. 2013. Cellular source and mechanisms of high transcriptome
892 complexity in the mammalian testis. *Cell Rep* **3**: 2179-2190.
893 Tan JHL, Wollmann H, van Pelt AMM, Kaldis P, Messerschmidt DM. 2020. Infertility-Causing
894 Haploinsufficiency Reveals TRIM28/KAP1 Requirement in Spermatogonia. *Stem Cell*
895 *Reports* **14**: 818-827.
896 Timms RT, Tchasovnikarova IA, Antrobus R, Dougan G, Lehner PJ. 2016. ATF7IP-Mediated
897 Stabilization of the Histone Methyltransferase SETDB1 Is Essential for Heterochromatin
898 Formation by the HUSH Complex. *Cell Rep* **17**: 653-659.
899 Tsusaka T, Fukuda K, Shimura C, Kato M, Shinkai Y. 2020. The fibronectin type-III (FNIII)
900 domain of ATF7IP contributes to efficient transcriptional silencing mediated by the
901 SETDB1 complex. *Epigenetics Chromatin* **13**: 52.

bioRxiv preprint doi: https://doi.org/10.1101/2023.09.30.560314; this version posted October 2, 2023. The copyright holder for this preprint (which was not certified by peer review) is the author/funder, who has granted bioRxiv a license to display the preprint in perpetuity. It is made available under aCC-BY-NC-ND 4.0 International license.

902 Tsusaka T, Shimura C, Shinkai Y. 2019. ATF7IP regulates SETDB1 nuclear localization and
903 increases its ubiquitination. *EMBO Rep* **20**: e48297.
904 Turner JM. 2015. Meiotic Silencing in Mammals. *Annu Rev Genet* **49**: 395-412.
905 van der Heijden GW, Derijck AA, Pósfai E, Giele M, Pelczar P, Ramos L, Wansink DG, van der
906 Vlag J, Peters AH, de Boer P. 2007. Chromosome-wide nucleosome replacement and
907 H3.3 incorporation during mammalian meiotic sex chromosome inactivation. *Nat Genet*
908 **39**: 251-258.
909 Yeh YH, Hu M, Nakagawa T, Sakashita A, Yoshida S, Maezawa S, Namekawa SH. 2021.
910 Isolation of Murine Spermatogenic Cells using a Violet-Excited Cell-Permeable DNA
911 Binding Dye. *J Vis Exp*.
912 Yoshida K, Maekawa T, Ly NH, Fujita SI, Muratani M, Ando M, Katou Y, Araki H, Miura F,
913 Shirahige K et al. 2020. ATF7-Dependent Epigenetic Changes Are Required for the
914 Intergenerational Effect of a Paternal Low-Protein Diet. *Mol Cell* **78**: 445-458.e446.
915

bioRxiv preprint doi: https://doi.org/10.1101/2023.09.30.560314; this version posted October 2, 2023. The copyright holder for this preprint (which was not certified by peer review) is the author/funder, who has granted bioRxiv a license to display the preprint in perpetuity. It is made available under aCC-BY-NC-ND 4.0 International license.

Alavattam_Fig1

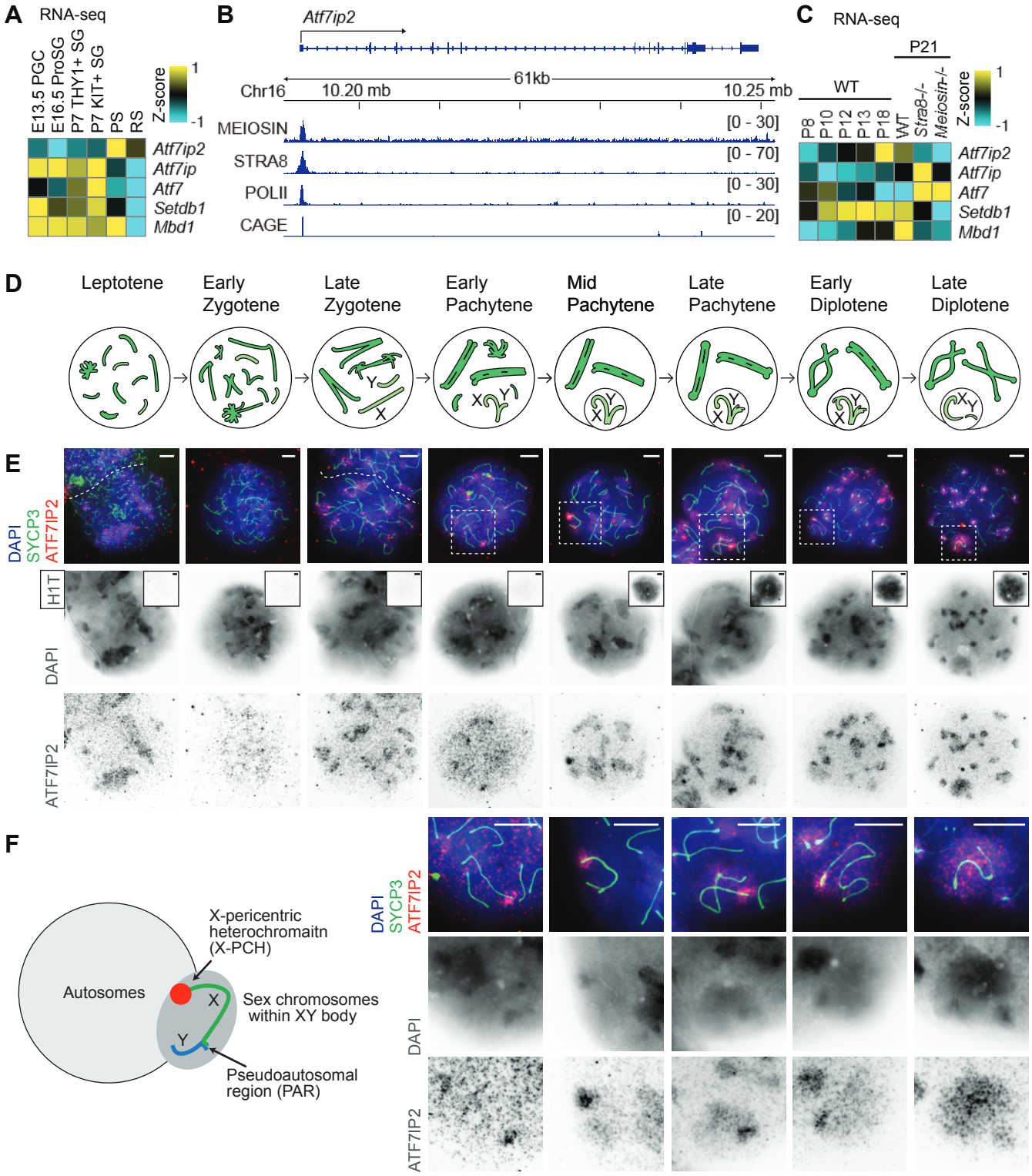

bioRxiv preprint doi: https://doi.org/10.1101/2023.09.30.560314; this version posted October 2, 2023. The copyright holder for this preprint (which was not certified by peer review) is the author/funder, who has granted bioRxiv a license to display the preprint in perpetuity. It is made available under aCC-BY-NC-ND 4.0 International license.

Alavattam_Fig2

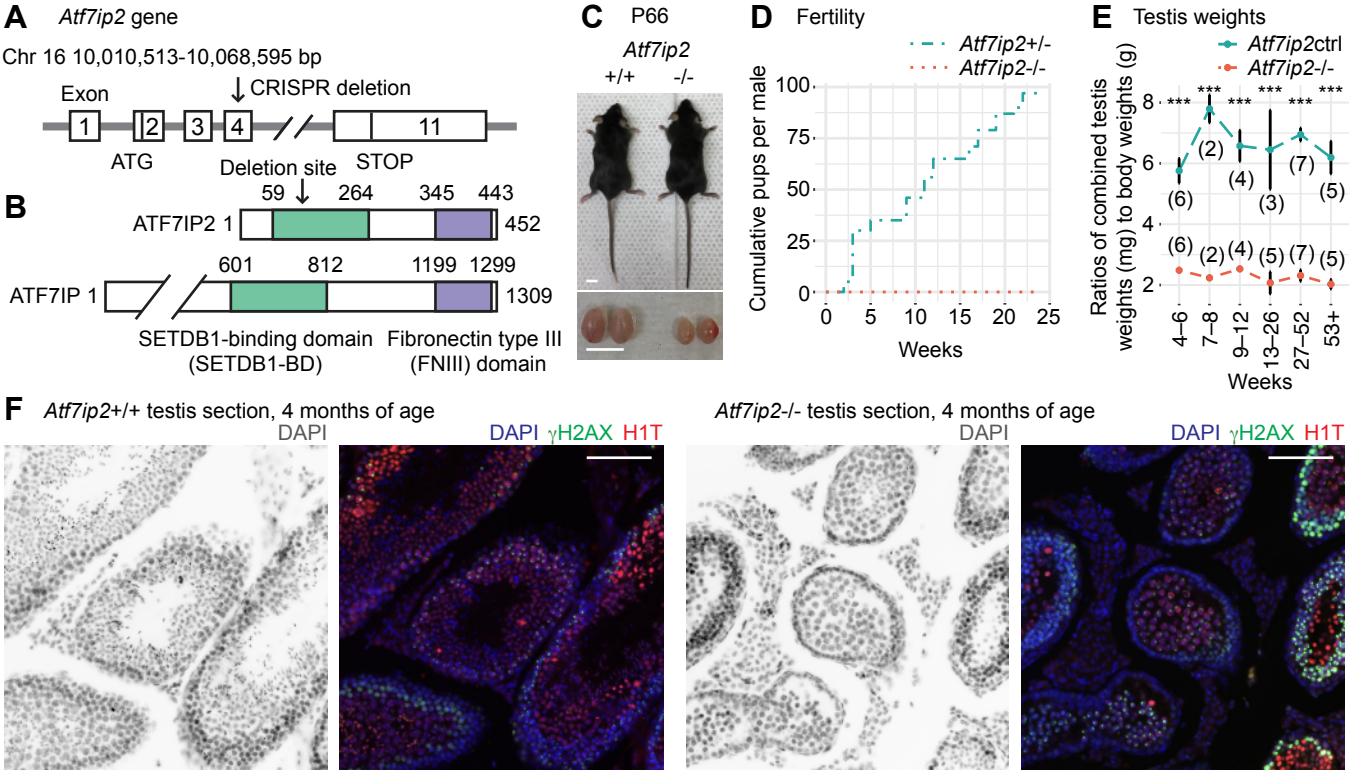

bioRxiv preprint doi: https://doi.org/10.1101/2023.09.30.560314; this version posted October 2, 2023. The copyright holder for this preprint (which was not certified by peer review) is the author/funder, who has granted bioRxiv a license to display the preprint in perpetuity. It is made available under aCC-BY-NC-ND 4.0 International license.

Alavattam_Fig3

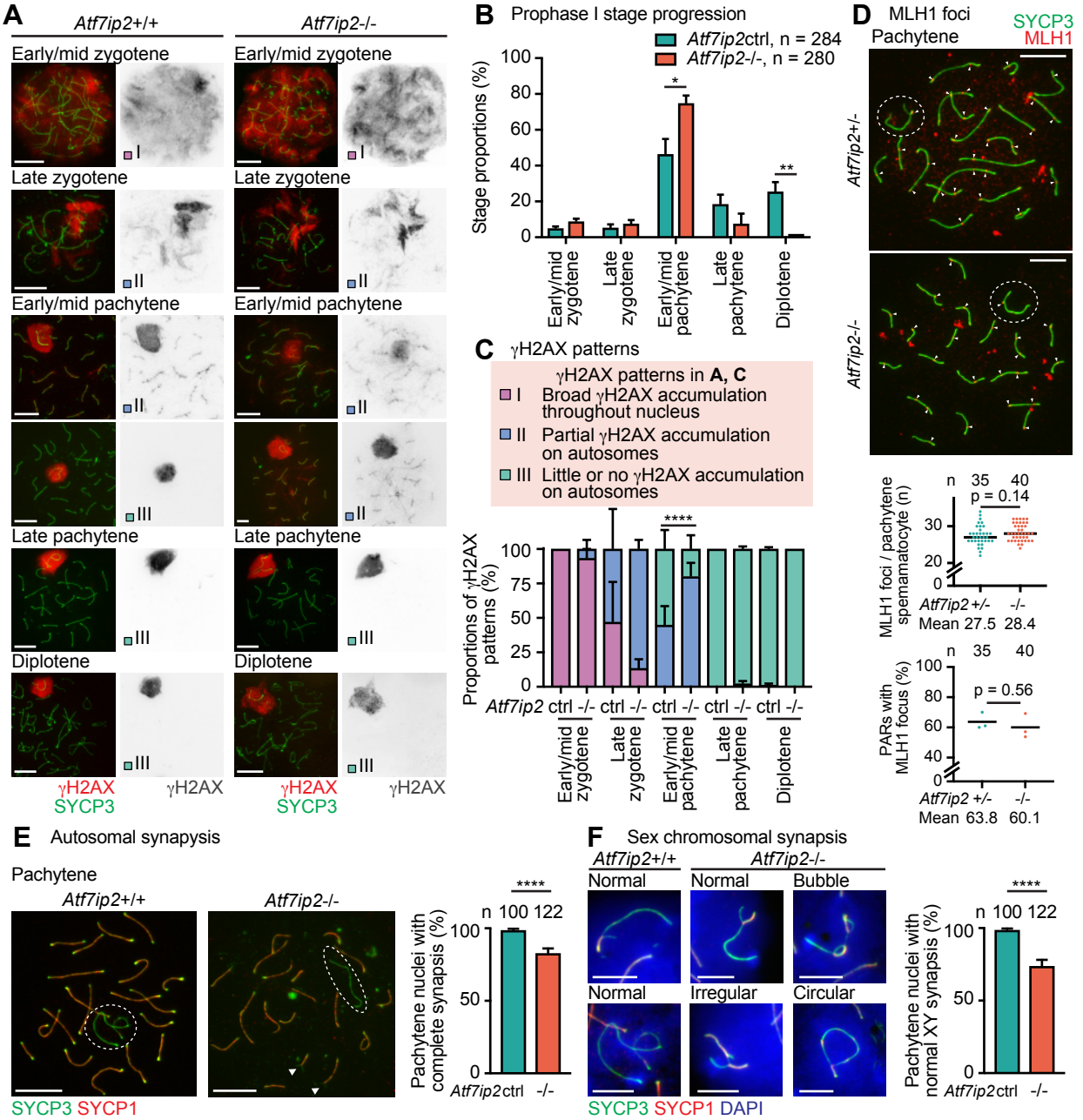

bioRxiv preprint doi: https://doi.org/10.1101/2023.09.30.560314; this version posted October 2, 2023. The copyright holder for this preprint (which was not certified by peer review) is the author/funder, who has granted bioRxiv a license to display the preprint in perpetuity. It is made available under aCC-BY-NC-ND 4.0 International license.

Alavattam_Fig4

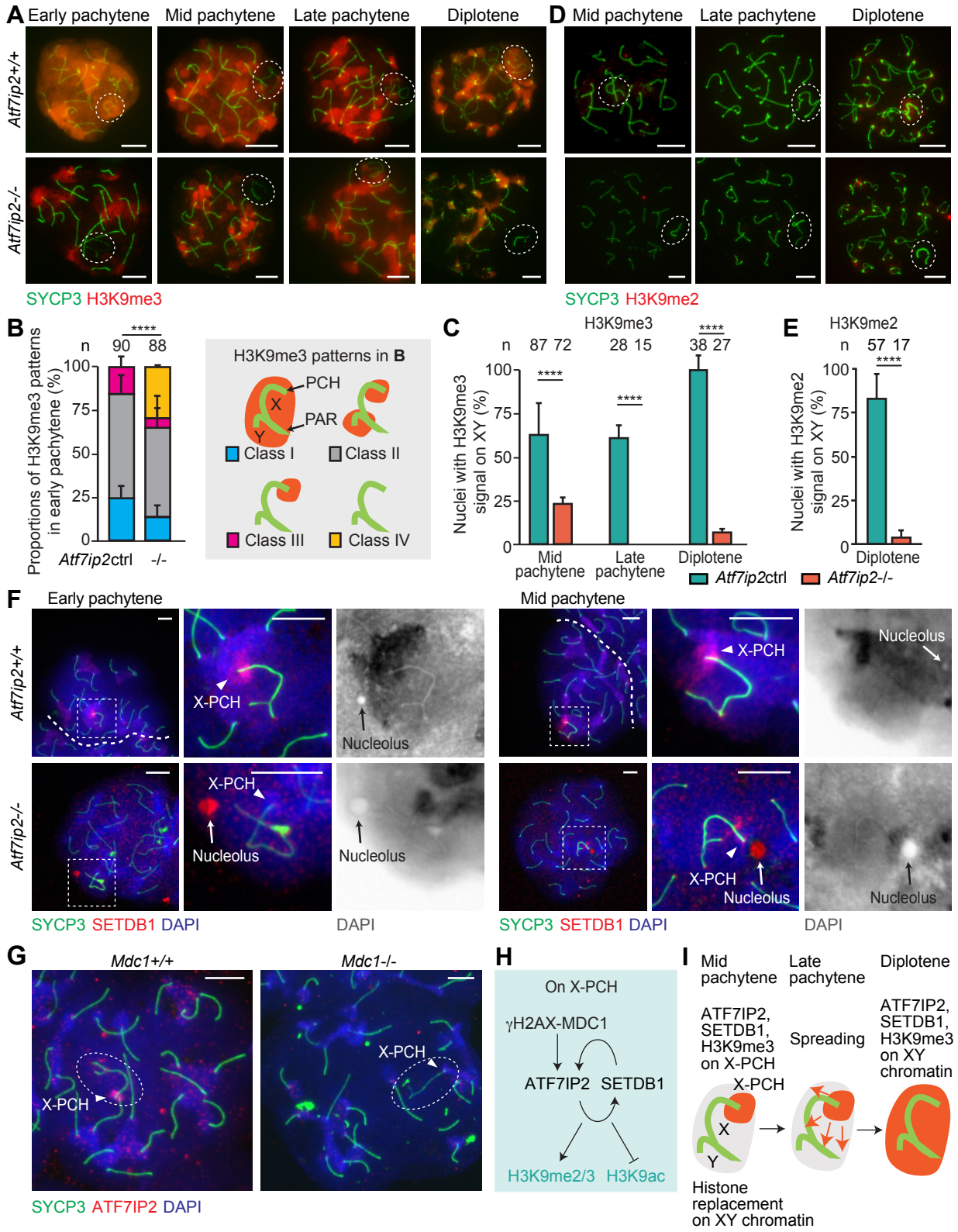

bioRxiv preprint doi: https://doi.org/10.1101/2023.09.30.560314; this version posted October 2, 2023. The copyright holder for this preprint (which was not certified by peer review) is the author/funder, who has granted bioRxiv a license to display the preprint in perpetuity. It is made available under aCC-BY-NC-ND 4.0 International license.

Alavattam_Fig5

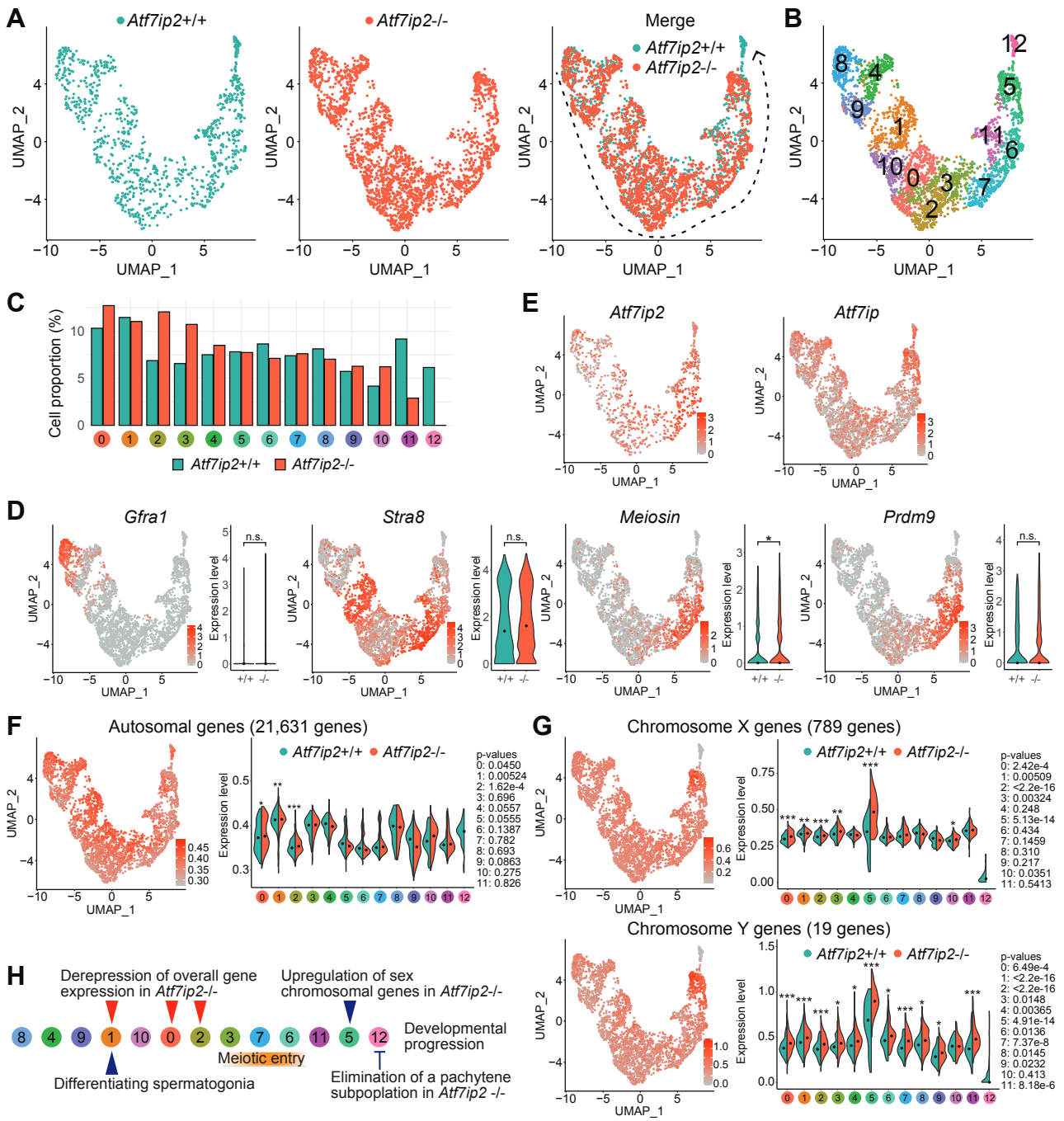

bioRxiv preprint doi: https://doi.org/10.1101/2023.09.30.560314; this version posted October 2, 2023. The copyright holder for this preprint (which was not certified by peer review) is the author/funder, who has granted bioRxiv a license to display the preprint in perpetuity. It is made available under aCC-BY-NC-ND 4.0 International license.

Alavattam_Fig6

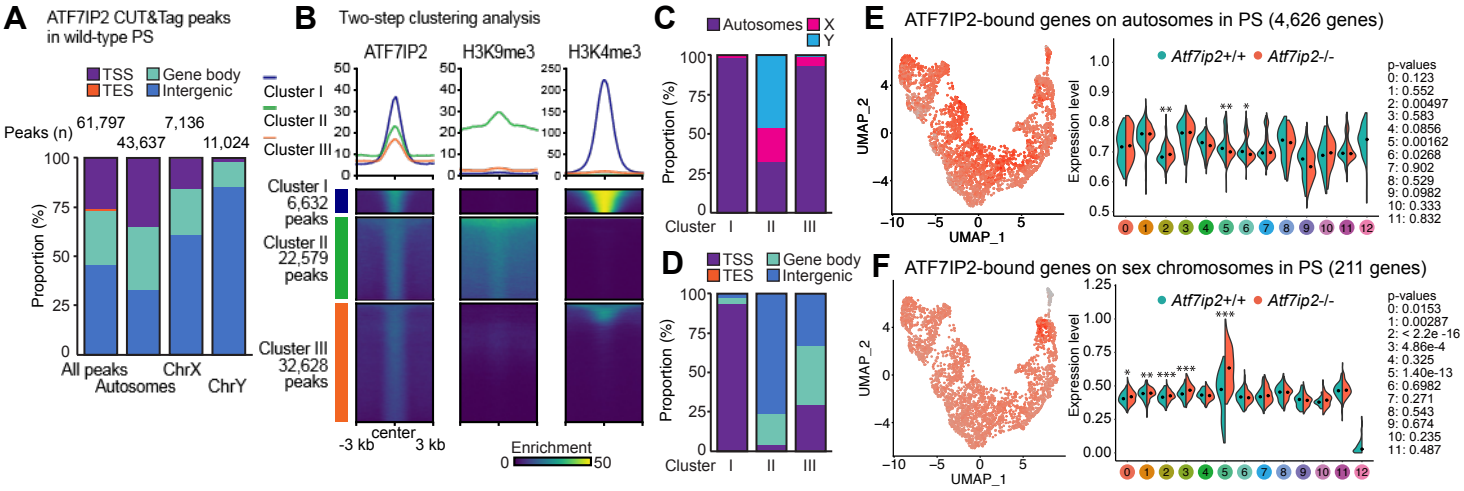

bioRxiv preprint doi: https://doi.org/10.1101/2023.09.30.560314; this version posted October 2, 2023. The copyright holder for this preprint (which was not certified by peer review) is the author/funder, who has granted bioRxiv a license to display the preprint in perpetuity. It is made available under aCC-BY-NC-ND 4.0 International license.
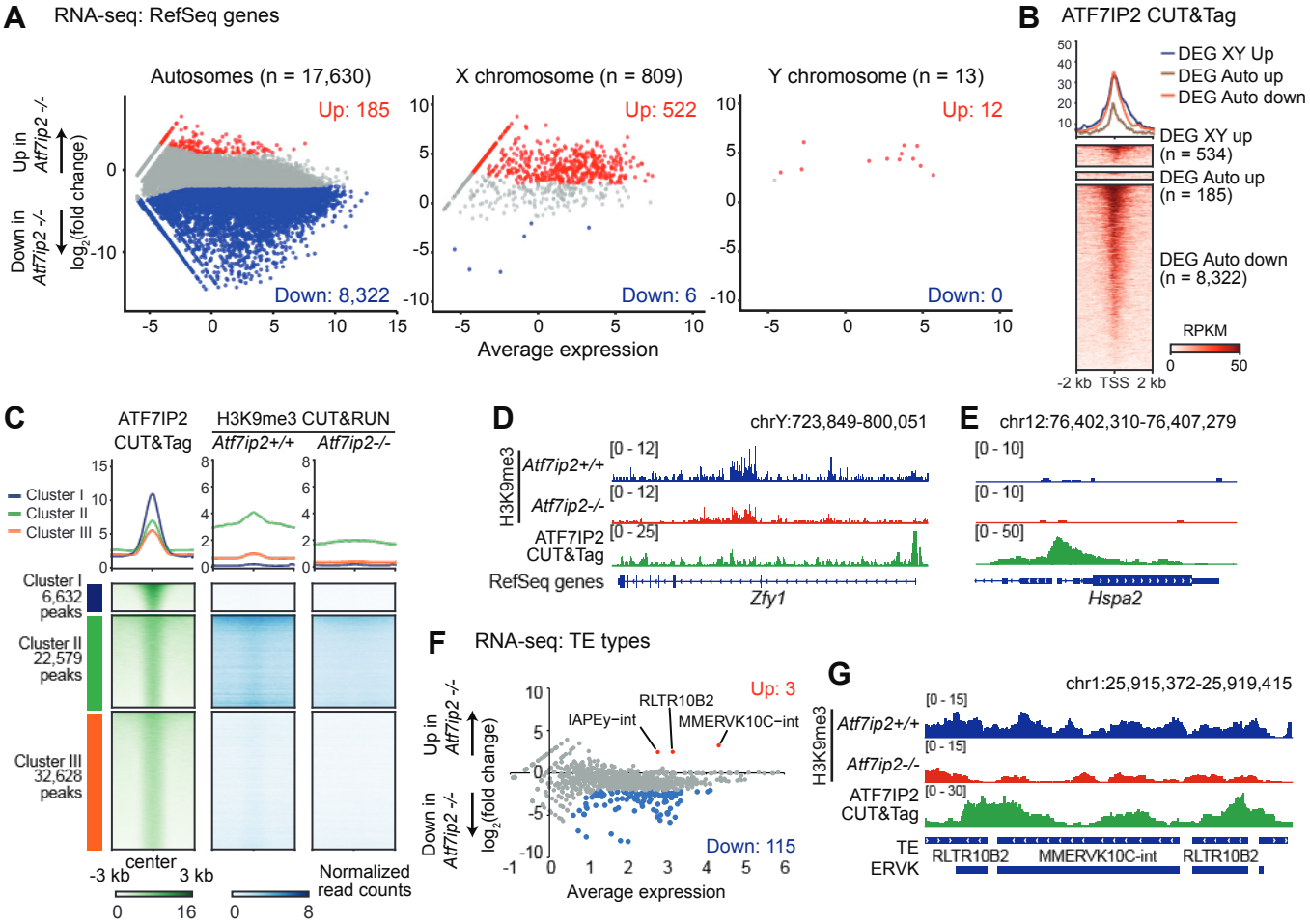
Alavattam_Fig7